J. Fluid Mech. (2002), *vol.* 451, *pp.* 1–33.
DOI: 10.1017/S0022112001006218 Printed in the United Kingdom

Bragg scattering of random surface gravity waves by irregular seabed topography

By FABRICE ARDHUIN[1,2] AND T. H. C. HERBERS[2]

[1]Centre Militaire d'Océanographie, Service Hydrographique et Océanographique de la Marine, 29275 Brest, France

[2]Department of Oceanography, Naval Postgraduate School, Monterey, CA, 93943-5122, USA

(Received 8 November 2000 and in revised form 23 June 2001)

The Bragg scattering of random, non-stationary surface gravity waves by random topography on a gently sloping bottom is investigated. A correction is given of previously published expressions for the triad wave–wave–bottom interaction source term in the spectral energy balance equation, and the result is reconciled with deterministic theories for the reflection of waves from sinusoidal seabed undulations. For both normal and oblique incidence, the stochastic and deterministic theories are equivalent in the limit of long propagation distances. Even for relatively short distances (for example two bottom undulations), the reflected energy predicted by the stochastic source term formulation is generally within 15% of values predicted by deterministic theories. The detuning of Bragg resonance by refraction and shoaling is discussed, suggesting practical validity conditions for the stochastic theory. The effect of bottom scattering on swell propagation is illustrated with numerical model computations for the North Carolina continental shelf using high-resolution bathymetry and an efficient semi-implicit scheme to evaluate the bottom scattering source term and integrate the energy balance equation. Model results demonstrate the importance of forward scattering of waves that propagate at large oblique angles over bottom features with typical scales of one to several surface wavelengths. This process contributes significantly to the directional spread of swell on the continental shelf by diffusing energy, in the spectrum, around the mean wave direction. Back-scattering, caused by bottom features with crests parallel to those of the surface waves and wavelengths close to half the surface wavelength, is weak, owing to the sharp roll-off of the bottom elevation spectrum at high wavenumbers. Model predictions are consistent with field measurements.

1. Introduction

Many theories have been proposed that describe the effects of natural depth variations on the propagation of surface gravity waves over a continental shelf or in a shallow marginal sea. The importance of wave refraction and shoaling caused by large-scale features (i.e. many surface wavelengths) such as submarine shoals and canyons, islands, bays and headlands is well known (Munk & Traylor 1947), and these effects are well described by numerical models (see for example O'Reilly & Guza 1993). The effects of depth variations with intermediate scales of the order of the surface wavelength are less well understood.

Hasselmann (1966) proposed a statistical theory for the evolution of random surface gravity waves over an irregular bottom, assuming spatially homogeneous conditions

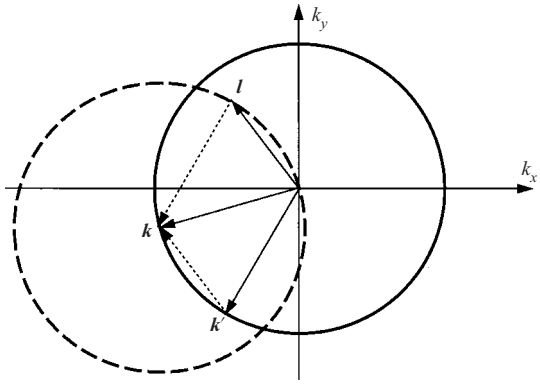

FIGURE 1. Geometric properties of wavenumbers satisfying the resonance condition. The interaction between a surface wave with wavenumber $\boldsymbol{k}'$ and a bottom component with wavenumber $\boldsymbol{l}$ excites a surface wave with the sum wavenumber $\boldsymbol{k} = \boldsymbol{k}' + \boldsymbol{l}$. For fixed $\boldsymbol{k}$, the resonant $\boldsymbol{k}'$ and $\boldsymbol{l}$ lie on the solid and dashed circles, respectively.

(i.e. uniform surface wave and bottom elevation spectra). At the lowest order, two wave components with the same radian frequency ω but different wavenumber vectors $\boldsymbol{k}$ and $\boldsymbol{k}'$ exchange energy in a resonant triad interaction with the bottom component that has the difference wavenumber $\boldsymbol{l} = \boldsymbol{k} - \boldsymbol{k}'$ (figure 1). This process is potentially important for the directional properties of the waves. Long (1973) applied Hasselmann's theory to swell in the North Sea with some assumptions about the unknown statistical properties of the bottom topography. His results suggested that back scattering of surface waves from bottom undulations with wavelengths close to half the surface wavelength ($\boldsymbol{k} \approx -\boldsymbol{k}'$, $\boldsymbol{l} \approx 2\boldsymbol{k}$) could explain the swell energy decay observed during the JONSWAP experiment (Hasselmann *et al.* 1973). Subsequent bathymetric surveys (Richter, Schmalfeldt & Siebert 1976) showed that the amplitude of seabed undulations at the site of the JONSWAP experiment was too small to cause significant back scattering. Although the potential importance of wave–bottom scattering is widely recognised (see for example Mei & Liu 1993), the lack of detailed bathymetric data has prevented further investigations of this process over natural seabed topography (Komen *et al.* 1994).

Different deterministic theories have been developed for wave reflection by periodic bottom undulations. Davies (1979) derived an analytical solution for the weak reflection of a monochromatic wavetrain propagating at normal incidence over a patch of sinusoidal bars, that was subsequently verified in laboratory experiments (Heathershaw 1982; Davies & Heathershaw 1984). Davies' theory does not account for the decay of the incident wave, losing energy to the reflected component, and therefore overestimates strong reflections, in particular at resonance where $\boldsymbol{l} = 2\boldsymbol{k}$. Mei (1985) derived a more accurate energy conserving solution, valid close to resonance, that was confirmed by experiments (Hara & Mei 1987). The more general case of oblique incidence was considered by Mei (1985), Dalrymple & Kirby (1986) and Kirby (1993). Mei (1985) further generalized his theory to bars superimposed on a sloping bottom. Kirby (1986*a*, *b*) subsequently showed that Mei's (1985) generalized theory can also be derived from modified mild slope equations. Other related developments include nonlinear effects in a long-wave approximation (Benjamin, Boczar-Karakiewicz & Pritchard 1987), higher-order Bragg scattering (Mitra & Greenberg 1984; Belzons, Rey & Guazzelli 1991; Liu & Yue 1998; Agnon & Sheremet 2000), extended mild

slope equations for steep topography (Athanassoulis & Belibakis 1999), and investigations of Anderson localization of waves on a random bottom (Devillard, Dunlop & Souillard 1988; Belzons, Guazzelli & Parodi 1988). Implications for sediment transport and the formation of multiple sand bar systems just outside the surf zone were discussed by Heathershaw (1982), Mei (1985) and Dulou, Belzons & Rey (2000).

Whereas Hasselmann's (1966) stochastic theory gives an energy balance equation that is an efficient tool for predicting the spectral evolution of random waves, it is restricted to homogeneous wave and bottom topography properties, and has not been verified experimentally. In contrast, Mei's (1985) deterministic theory is more general and has been verified for simple cases, but it has not yet been applied to a natural seabed because it requires a numerical solution to an elliptic equation that is prohibitively expensive for large domains. Kirby (1986*a*) discussed these two complementary theories but could not reconcile them for the case of monochromatic waves travelling over a sinusoidal bottom. Indeed, Hasselmann's theory assumes that the wave energy spectrum is continuous across the resonance manifold in order to determine its long-term evolution, and thus cannot be applied to monochromatic waves (see Hasselmann 1962 and Komen *et al.* 1994 for detailed discussions of the continuum approximation in random wave scattering theory).

In this paper, we examine the effects of wave scattering from natural seabed topography by extending Hasselmann's (1966) theory to heterogeneous waves and bottoms. In § 2 we rederive Hasselmann's scattering source term on a gently sloping bottom with slowly varying wave and bottom spectral properties, correcting for an apparent error in the wave–bottom coupling coefficients given by Hasselmann (1966) and Long (1973). In § 3 the predicted scattering source term for a sinusoidal bottom is shown to be in agreement with the well-verified solutions of deterministic theories. The effects of Bragg scattering on swell propagation across the North Carolina continental shelf are illustrated in § 4 with an implementation of the scattering source term in the spectral wave prediction model CREST (Ardhuin, Herbers & O'Reilly 2001) using measured wave spectra and high-resolution bathymetric data. Conclusions are given in § 5.

2. Scattering theory for random waves in heterogeneous conditions

The present derivation of the energy balance equation for random waves propagating over an irregular sea floor uses a perturbation expansion of the wave energy, closely following Hasselmann's (1962) derivation of energy transfers in quartet wave–wave interactions, and a ray approximation of medium variations adapted from Mei (1989, ch. 3). The result is a local energy balance equation that incorporates refraction and shoaling by large-scale depth variations, and a source term describing Bragg scattering by seabed topography with small horizontal scales (of the order of the surface wavelength).

2.1. *General formulation*

We consider weakly nonlinear random waves propagating over an irregular bottom with a slowly varying mean depth and random small-scale topography. For the sake of simplicity, we will neglect the effects of mean currents on wave propagation (see for example Bretherton & Garrett 1969) and on wave scattering by bottom undulations (Kirby 1988). All variables are non-dimensionalized with a representative wavenumber k_0, acceleration due to gravity g and water density ρ. The bottom elevation is represented by $z = -H(\boldsymbol{x}) + h(\boldsymbol{x})$, where h is a zero-mean small deviation

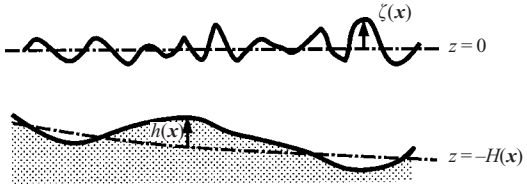

FIGURE 2. Definition sketch.

from the gently sloping large-scale bottom features represented by $-H(\boldsymbol{x})$, $\boldsymbol{x}$ is the horizontal position vector, and z is the elevation relative to the mean water level. The vertical position of the ocean free surface is given by $\zeta(\boldsymbol{x}, t)$ with a zero mean value (figure 2). Assuming irrotational flow for an incompressible fluid, the horizontal velocity field $\boldsymbol{u}$ is equal to $\nabla\phi$, the horizontal gradient of a velocity potential, and the vertical velocity w is equal to $\partial\phi/\partial z$. We further assume that ρ is constant. The governing equations for ϕ are

$$\nabla^2\phi + \frac{\partial^2\phi}{\partial z^2} = 0 \quad \text{for} \quad -H + h \leqslant z \leqslant \zeta, \tag{2.1}$$

$$\frac{\partial\phi}{\partial z} = \nabla\phi \cdot (\nabla h - \nabla H) \quad \text{at} \quad z = -H + h, \tag{2.2}$$

$$\frac{\partial^2\phi}{\partial t^2} + \frac{\partial\phi}{\partial z} = \nabla\phi \cdot \nabla\zeta - \nabla\phi \cdot \frac{\partial\nabla\phi}{\partial t} - \frac{\partial\phi}{\partial z}\frac{\partial^2\phi}{\partial t\partial z} \quad \text{at} \quad z = \zeta. \tag{2.3}$$

Equation (2.1) is Laplace's equation, (2.2) is the 'free slip' bottom boundary condition, and the 'combined' surface boundary condition (2.3) is obtained by eliminating linear terms involving ζ from the dynamic (i.e. Bernoulli's equation) and kinematic conditions at the free surface (see for example Hasselmann 1962). ζ is given by Bernoulli's equation,

$$\zeta + \frac{\partial\phi}{\partial t} = -\frac{1}{2}\left[|\nabla\phi|^2 + \left(\frac{\partial\phi}{\partial z}\right)^2\right] \quad \text{at} \quad z = \zeta. \tag{2.4}$$

Assuming that h varies on scales of the order of the surface wavelength, we introduce three small parameters: the wave slope $\varepsilon = k_0 a_0$, the small-scale bottom slope $\eta = k_0 h_0$, and a measure β of the large-scale bottom slope $|\nabla H|$. Equations (2.1)–(2.3) are scaled as

$$\nabla^2\phi + \frac{\partial^2\phi}{\partial z^2} = 0 \quad \text{for} \quad (-H + \eta h) \leqslant z \leqslant \varepsilon\zeta, \tag{2.5}$$

$$\frac{\partial\phi}{\partial z} = \nabla\phi \cdot (\eta\nabla h - \beta\nabla H) \quad \text{at} \quad z = -H + \eta h, \tag{2.6}$$

$$\frac{\partial^2\phi}{\partial t^2} + \frac{\partial\phi}{\partial z} = \varepsilon\nabla\phi \cdot \nabla\zeta - \varepsilon\nabla\phi \cdot \frac{\partial\nabla\phi}{\partial t} - \varepsilon\frac{\partial\phi}{\partial z}\frac{\partial^2\phi}{\partial t\partial z} \quad \text{at} \quad z = \varepsilon\zeta. \tag{2.7}$$

Following Keller (1958) we introduce slow space $\tilde{\boldsymbol{x}} = \alpha\boldsymbol{x}$ and time $\tilde{t} = \gamma t$ variables. h and ϕ are assumed to be semi-stationary random processes in horizontal space and time (for ϕ only), with evolution scales $(\alpha k_0)^{-1}$ and $\gamma^{-1}k_0^{-1/2}$, respectively (Priestley 1965), that can be decomposed into Fourier modes with slowly varying amplitudes.

Following Hasselmann (1962) we shall approximate h and ϕ with discrete sums, and take the limit to continuous integrals after deriving expressions for the evolution of the phase averaged wave energy. We write

$$h(\boldsymbol{x}) = \sum_{\boldsymbol{l}} B_{\boldsymbol{l}}(\tilde{\boldsymbol{x}}) \mathrm{e}^{\mathrm{i}\boldsymbol{l}\cdot\boldsymbol{x}}, \tag{2.8}$$

where $\boldsymbol{l}$ are regularly spaced wavenumbers of bottom undulations and $B_{\boldsymbol{l}}$ are slowly varying amplitudes. Anticipating the effects of refraction, ϕ is decomposed as

$$\phi(\boldsymbol{x}, t) = \sum_{\boldsymbol{k}} \Phi_{\boldsymbol{k}}(\tilde{\boldsymbol{x}}, t, z) \mathrm{e}^{\mathrm{i}S_{\boldsymbol{k}}(\boldsymbol{x})}, \tag{2.9}$$

where $\boldsymbol{k}$ are regularly spaced surface wavenumbers, and each $\boldsymbol{k}$-component has an amplitude $\Phi_{\boldsymbol{k}}$, an eikonal $S_{\boldsymbol{k}}$, and a local wavenumber

$$\boldsymbol{k}_r(\boldsymbol{k}, \beta\boldsymbol{x}) = \nabla S_{\boldsymbol{k}}(\boldsymbol{x}) \tag{2.10}$$

such that $\boldsymbol{k}_r = \boldsymbol{k}$ at the origin $\boldsymbol{x} = \boldsymbol{0}$; $\Phi_{\boldsymbol{k}}$ and $\boldsymbol{k}_r$ are Lagrangian variables following a wave component along a ray trajectory. The spectral decomposition (2.9) for an evolutionary process is 'unique', in a sense defined by Priestley (1981, theorem 11.2.3), only for a finite region in space and time, and is used here only to evaluate local variations of $\Phi_{\boldsymbol{k}}$.

The slow spatial variations of $\Phi_{\boldsymbol{k}}$ can result from shoaling, refraction, and scattering processes, as well as non-stationary and non-uniform wave conditions. Since ϕ and h are real, it follows that $\overline{\Phi_{\boldsymbol{k}}} = \Phi_{-\boldsymbol{k}}$ and $\overline{B_{\boldsymbol{l}}} = B_{-\boldsymbol{l}}$, where the overbar denotes the complex conjugate.

In the vicinity of $\boldsymbol{x} = \boldsymbol{0}$, the decomposition (2.9) reduces to a Fourier sum

$$\phi(\boldsymbol{x}, t) = \sum_{\boldsymbol{k}} \Phi_{\boldsymbol{k}}(\boldsymbol{0}, t, z) \mathrm{e}^{\mathrm{i}\boldsymbol{k}\cdot\boldsymbol{x}} + O(\alpha|\boldsymbol{x}|, \beta|\boldsymbol{x}|). \tag{2.11}$$

The simplified decomposition (2.11) will be used when no space differentiation is involved, taking advantage of the orthogonality of Fourier modes.

The goal of the present derivation is to determine from (2.1)–(2.4) the energy balance at $\tilde{\boldsymbol{x}} = \boldsymbol{0}$ for each $\boldsymbol{k}$-component of the wave spectrum (2.9). The solution depends on the relative magnitudes of the five small parameters: α, β, γ, η and ε. Here, we use

$$\alpha \approx \beta \approx \gamma \approx \eta^2 \approx \varepsilon^2 \ll \boldsymbol{1}. \tag{2.12}$$

The choice of a small-scale bottom slope η much larger than the large-scale slope β is usually well suited to sandy continental shelves, with the exception of the steeper beach and shelf break regions. This choice makes the present derivation *a priori* different from Mei's (1985) theory in which $\alpha \approx \beta \approx \eta$.

Following the method of Hasselmann (1962), the solution to (2.5)–(2.7) is obtained through a perturbation expansion in powers of ε,

$$\phi = \phi_1 + \varepsilon\phi_2 + \varepsilon^2\phi_3 + \text{h. o. t.} \tag{2.13}$$

The boundary conditions (2.6) and (2.7) are expressed at $z = -H$ and $z = 0$, respectively, using Taylor series expansions of ϕ about $z = -H$ and $z = 0$, e.g. at the bottom,

$$\phi|_{z=-H+h} = \phi|_{z=-H} + \eta h \left.\frac{\partial\phi}{\partial z}\right|_{z=-H} + \eta^2 \frac{h^2}{2} \left.\frac{\partial^2\phi}{\partial z^2}\right|_{z=-H} + \text{h. o. t.} \tag{2.14}$$

Each term in (2.13) will be found to be of the form

$$\phi_i = \sum_{\boldsymbol{k},s} \frac{\cosh(k_r z + k_r H)}{\cosh(k_r H)} \Phi^s_{i,\boldsymbol{k}}(\tilde{\boldsymbol{x}}, t) \mathrm{e}^{\mathrm{i}S_{i,k}(\boldsymbol{x})} + \text{bound wave terms}, \tag{2.15}$$

where k_r is the magnitude of the local wavenumber vector $\boldsymbol{k}_r$, s is a sign index (+ or −), $\Phi^s_{i,\boldsymbol{k}}$ is the amplitude of the free wave component $(\boldsymbol{k}, s)$ that propagates in the direction of $s\boldsymbol{k}_r$, and $\overline{\Phi^s_{i,\boldsymbol{k}}} = \Phi^{-s}_{i,-\boldsymbol{k}}$.

The slowly evolving spectral statistics of free wave components can be expressed in terms of the covariances $F^{\Phi}_{i,j,\boldsymbol{k}}$ of the velocity potential amplitudes:

$$F^{\Phi}_{i,j,\boldsymbol{k}} = \left\langle \Phi^+_{i,\boldsymbol{k}} \Phi^-_{j,-\boldsymbol{k}} + \Phi^-_{i,-\boldsymbol{k}} \Phi^+_{j,\boldsymbol{k}} \right\rangle. \tag{2.16}$$

where the angular brackets denote an average over many realizations of the wave field, and in local space and time over a region that is large compared to the 'fast' scales k_0^{-1} of sea surface excursions, but small compared to the slow scales $(\alpha k_0)^{-1}$ and $\gamma^{-1}(k_0)^{-1/2}$ of spectral variations. The contribution of the complex conjugate pairs of components $(\boldsymbol{k}, +)$ and $(-\boldsymbol{k}, -)$ are combined in (2.16) so that $F_{i,j,\boldsymbol{k}}$ is the covariance of waves propagating in the direction of $\boldsymbol{k}$. Note that the wavenumber separations $\Delta\boldsymbol{k}_r = (\Delta k_{r,x}, \Delta k_{r,y})$ in the sum (2.9) vary along rays owing to refraction. In the limit of small wavenumber separation, a continuous cross-spectrum can be defined at $\tilde{\boldsymbol{x}}$ (e.g. Priestley 1981, ch. 11)

$$F^{\Phi}_{i,j}(\tilde{\boldsymbol{x}}, \tilde{t}, \boldsymbol{k}) = \lim_{|\Delta\boldsymbol{k}|\to 0} \frac{F^{\Phi}_{i,j,\boldsymbol{k}}(\tilde{\boldsymbol{x}}, \tilde{t})}{\Delta k_x \Delta k_y}. \tag{2.17}$$

The definitions of all spectral densities are chosen so that the integral over the entire wavenumber plane yields the total covariance of ϕ_i and ϕ_j.

The slowly varying bottom elevation spectrum in discrete form is given by $F^B_{\boldsymbol{l}} = \langle B_{\boldsymbol{l}} B_{-\boldsymbol{l}} \rangle$ and in continuous form by

$$F^B(\tilde{\boldsymbol{x}}, \boldsymbol{l}) = \lim_{|\Delta\boldsymbol{l}|\to 0} \frac{F^B_{\boldsymbol{l}}(\tilde{\boldsymbol{x}})}{\Delta_{lx}\Delta_{ly}}, \tag{2.18}$$

so that

$$\langle h^2(\tilde{\boldsymbol{x}}) \rangle = \int_{-\infty}^{+\infty} \int_{-\infty}^{+\infty} F^B(\tilde{\boldsymbol{x}}, \boldsymbol{l})\, \mathrm{d}l_x \mathrm{d}l_y. \tag{2.19}$$

This definition differs by a factor of 2 from that chosen by Hasselmann (1966) and Long (1973).

The total wave energy at $\tilde{\boldsymbol{x}} = \boldsymbol{0}$, in non-dimensional form,

$$E(\boldsymbol{0}, \tilde{t}) = \left\langle \int_{-H+h}^{\zeta} \frac{1}{2} \left[|\nabla\phi|^2 + \left(\frac{\partial\phi}{\partial z} \right)^2 \right] \mathrm{d}z \right\rangle + \frac{1}{2} \langle \zeta^2 \rangle, \tag{2.20}$$

can be written as

$$E(\boldsymbol{0}, \tilde{t}) = \int_{-\infty}^{\infty} \int_{-\infty}^{\infty} \left[\varepsilon^2 E_2(\boldsymbol{k}) + \varepsilon^3 E_3(\boldsymbol{k}) + \varepsilon^4 E_4(\boldsymbol{k}) \right] \mathrm{d}k_x \mathrm{d}k_y + O(\varepsilon^5), \tag{2.21}$$

where

$$E_2(\boldsymbol{k}) = E_{1,1}(\boldsymbol{k}), \tag{2.22}$$

$$E_3(\boldsymbol{k}) = E_{2,1}(\boldsymbol{k}) + E_{1,2}(\boldsymbol{k}), \tag{2.23}$$

$$E_4(\boldsymbol{k}) = E_{2,2}(\boldsymbol{k}) + E_{3,1}(\boldsymbol{k}) + E_{1,3}(\boldsymbol{k}). \tag{2.24}$$

Here, $E_{i,j}(\boldsymbol{k})$ is the $(i+j)$th order energy contribution from correlations between ith and jth-order components with wavenumber $\boldsymbol{k}$. Since the average in (2.20) is over several wavelengths, correlations between wave components with different wavenumbers that result from reflections (i.e. standing wave patterns of nodes and antinodes) are averaged out and do not contribute to (2.21). For all (i, j) pairs, $E_{i,j}(\boldsymbol{k}) = E_{j,i}(\boldsymbol{k})$. Hasselmann (1962) discarded odd-power energy terms E_3 and E_5 under the assumption that the sea surface is Gaussian. It was later found that this assumption is unnecessary (Benney & Saffman 1966; Newell & Aucoin 1971) as dispersion decorrelates the wave components during their propagation. Here, additional terms involving correlations between two wave and one bottom component contribute to E_3, but these terms are shown to be bounded in Appendix A. The dynamically important growing terms will be found in the 4th-order energy E_4 (2.24).

For freely propagating waves, the potential and kinetic energy contributions to (2.20) are equal and $E_{i,j}$ is approximately given by the linear relation

$$E_{i,j}(\mathbf{0}, \tilde{t}, \boldsymbol{k}) = kF^{\Phi}_{i,j}\left(\mathbf{0}, \tilde{t}, \boldsymbol{k}\right)\tanh(kH). \tag{2.25}$$

Neglected in (2.25) are the contributions to the kinetic energy integral (2.20) from the z-intervals $[-H + h, -H]$ and $[0, \zeta]$. Although these contributions are $O(\varepsilon^4)$ for $E_{1,1}$ and thus should be included in E_4, their magnitude is bounded and thus their time derivative is $O(\varepsilon^6)$. All $O(\varepsilon^4)$ bounded terms resulting from the surface and bottom boundary conditions can be discarded in the following analysis of energy transfers within the wave spectrum (see Hasselmann 1962 for a detailed discussion).

2.2. *First-order solution*

Substitution of the first-order wave field ϕ_1

$$\phi_1 = \sum_{\boldsymbol{k},s} \frac{\cosh(k_r z + k_r H)}{\cosh(k_r H)} \Phi^s_{1,\boldsymbol{k}}(\tilde{\boldsymbol{x}}, t)\mathrm{e}^{\mathrm{i}S_{1,\boldsymbol{k}}(\boldsymbol{x})} \tag{2.26}$$

in the surface boundary condition (2.7) yields

$$\Phi^s_{1,\boldsymbol{k}}(\tilde{\boldsymbol{x}}, t) = \widehat{\Phi}^s_{1,\boldsymbol{k}}(\tilde{\boldsymbol{x}}, \tilde{t})\mathrm{e}^{-\mathrm{i}s\omega t}, \tag{2.27}$$

where the radian frequency $\omega(k)$ is constant along rays, and is given by the linear dispersion relation (in non-dimensional form):

$$\omega(k) = [k_r \tanh(k_r H)]^{1/2}. \tag{2.28}$$

The slow space and time modulations of $\widehat{\Phi}^s_{1,\boldsymbol{k}}$ and the associated variations of the energy spectrum $E_2(\boldsymbol{k}_r)$ are not constrained by the first-order equations, but can be determined from the fourth-order energy $E_4(\boldsymbol{k}_r)$ (2.24), that depends on both second- and third-order waves.

2.3. *Second-order solution*

Substituting (2.13) in (2.5)–(2.7) and collecting terms of order ε and η yields the governing equations for the second-order velocity potential ϕ_2

$$\nabla^2\phi_2 + \frac{\partial^2\phi_2}{\partial z^2} = 0 \quad \text{for} \quad -H \leqslant z \leqslant 0, \tag{2.29}$$

$$\frac{\partial\phi_2}{\partial z} = -h\frac{\partial^2\phi_1}{\partial z^2} + \nabla\phi_1 \cdot \nabla h \quad \text{at} \quad z = -H, \tag{2.30}$$

$$\frac{\partial^2\phi_2}{\partial t^2} + \frac{\partial\phi_2}{\partial z} = NL_2 \quad \text{at} \quad z = 0, \tag{2.31}$$

where NL_2 contains the nonlinear terms in the surface boundary condition that force a bound wave solution ϕ_2^{nl} (Hasselmann 1962 (47)). Note that refraction and shoaling terms associated with the large-scale bottom slope ∇H are of higher order and do not contribute to the second-order equations. Therefore, ray curvature effects on ϕ_1 can be neglected, and we can use $\boldsymbol{k}_r \approx \boldsymbol{k}$ and $S_{\boldsymbol{k}}(\boldsymbol{x}) \approx \boldsymbol{k}\cdot\boldsymbol{x}$ in the vicinity of $\boldsymbol{x}=\boldsymbol{0}$. A general solution to Laplace's equation (2.29) is formed with a Fourier sum of free and bound wave components with amplitudes $\Phi^s_{2,\boldsymbol{k}}$ and $\Phi^{\mathrm{si},s}_{2,\boldsymbol{k}}$:

$$\phi_2 = \sum_{\boldsymbol{k},s}\left[\frac{\cosh(kz+kH)}{\cosh(kH)}\Phi^s_{2,\boldsymbol{k}}(t)+\frac{\sinh(kz+kH)}{\cosh(kH)}\Phi^{\mathrm{si},s}_{2,\boldsymbol{k}}(t)\right]\mathrm{e}^{\mathrm{i}\boldsymbol{k}\cdot\boldsymbol{x}}+\phi_2^{\mathrm{nl}}, \tag{2.32}$$

$\Phi^{\mathrm{si},s}_{2,\boldsymbol{k}}$ follows from substituting the first-order wave field ((2.26) and (2.27)) in the right-hand side of the bottom boundary condition (2.30).

$$\Phi^{\mathrm{si},s}_{2,\boldsymbol{k}}(t) = -\sum_{\boldsymbol{k}'}\frac{\boldsymbol{k}\cdot\boldsymbol{k}'}{k}B_{\boldsymbol{k}-\boldsymbol{k}'}\widehat{\Phi}^s_{1,\boldsymbol{k}'}\mathrm{e}^{-\mathrm{i}s\omega' t}, \tag{2.33}$$

where $(\omega', \boldsymbol{k}')$ obey the dispersion relation (2.28). The bound wave $\Phi^{\mathrm{si},s}_{2,\boldsymbol{k}}$ effectively couples the bottom and surface waves. Substitution of (2.32) and (2.33) in (2.31) yields a forced harmonic oscillator equation for the free wave amplitude $\Phi^s_{2,\boldsymbol{k}}$,

$$\left(\frac{\mathrm{d}}{\mathrm{d}t^2}+\omega^2\right)\Phi^s_{2,\boldsymbol{k}}(t) = \sum_{\boldsymbol{k}'}\left[k-\omega'^2\tanh(kH)\right]\frac{\boldsymbol{k}\cdot\boldsymbol{k}'}{k}B_{\boldsymbol{k}-\boldsymbol{k}'}\Phi^s_{1,\boldsymbol{k}'}(t). \tag{2.34}$$

Following the method of Hasselmann (1962), the time derivative of the energy density $E_{2,2}(\boldsymbol{k})$ of the second-order waves in the limit of large t at $\tilde{\boldsymbol{x}}=\boldsymbol{0}$, can be written in the form (Appendix A)

$$\frac{\partial E_{2,2}(\boldsymbol{k})}{\partial t} = K(k,H)\int_0^{2\pi}\cos^2(\theta-\theta')F^B(\boldsymbol{k}-\boldsymbol{k}')E_2(\boldsymbol{k}')\,\mathrm{d}\theta', \tag{2.35}$$

where $\boldsymbol{k}=(k\cos\theta, k\sin\theta)$, $\boldsymbol{k}'=(k\cos\theta', k\sin\theta')$, and

$$K(k,\,H) = \frac{4\pi\omega k^4}{\sinh(2kH)[2kH+\sinh(2kH)]}. \tag{2.36}$$

2.4. *Third-order solution*

Slow modulations of ϕ_1 yield third-order terms in Laplace's equation. Substituting (2.13), (2.26) and (2.27) in (2.5)–(2.7), collecting terms of order ε^2, $\varepsilon\eta$, η^2, α, β and γ, and using the approximations (in the vicinity of $\boldsymbol{x}=\boldsymbol{0}$) $\boldsymbol{k}_r = \boldsymbol{k}+O(\beta\boldsymbol{x})$, and $S_{\boldsymbol{k}}(\boldsymbol{x}) = \boldsymbol{k}\cdot\boldsymbol{x}+O(\alpha\boldsymbol{x},\,\beta\boldsymbol{x})$, yield the following equations for the third-order velocity potential ϕ_3

$$\nabla^2\phi_3+\frac{\partial^2\phi_3}{\partial z^2} = \overbrace{-\mathrm{i}\sum_{\boldsymbol{k},s}\boldsymbol{k}\cdot\nabla\left(\widehat{\Phi}^s_{1,\boldsymbol{k}}\frac{\cosh(k_rz+k_rH)}{\cosh(k_rH)}\right)\mathrm{e}^{\mathrm{i}(\boldsymbol{k}\cdot\boldsymbol{x}-s\omega t)}}^{\mathrm{I}}$$
$$\overbrace{-\mathrm{i}\sum_{\boldsymbol{k},s}\nabla\cdot\left(\boldsymbol{k}_r\widehat{\Phi}^s_{1,\boldsymbol{k}}\frac{\cosh(k_rz+k_rH)}{\cosh(k_rH)}\right)\mathrm{e}^{\mathrm{i}(\boldsymbol{k}\cdot\boldsymbol{x}-s\omega t)}}^{\mathrm{II}} \quad \text{for} \quad -H\leqslant z\leqslant 0, \tag{2.37}$$

$$\frac{\partial \phi_3}{\partial z} = -\overbrace{h\frac{\partial^2 \phi_2}{\partial z^2}}^{\text{III}} + \overbrace{\nabla\phi_2 \cdot \nabla h}^{\text{IV}} - \mathrm{i}\overbrace{\sum_{\boldsymbol{k},s} \boldsymbol{k}\cdot\nabla H \widehat{\Phi}^s_{1,\boldsymbol{k}} \mathrm{e}^{\mathrm{i}(\boldsymbol{k}\cdot\boldsymbol{x}-s\omega t)}}^{\text{V}} \quad \text{at} \quad z=-H, \tag{2.38}$$

$$\frac{\partial^2 \phi_3}{\partial t^2} + \frac{\partial \phi_3}{\partial z} = \mathrm{i}\overbrace{\sum_{\boldsymbol{k},s} 2s\omega \frac{\partial \widehat{\Phi}^s_{1,\boldsymbol{k}}}{\partial \tilde{t}} \mathrm{e}^{\mathrm{i}(\boldsymbol{k}\cdot\boldsymbol{x}-s\omega t)}}^{\text{VI}} + NL_3 \quad \text{at} \quad z=0. \tag{2.39}$$

Note that third-order terms involving ϕ_1 in the bottom boundary condition (2.38) vanish because $\partial^3\phi_1/\partial z^3 = 0$ and $\partial\phi_1/\partial z = 0$ at $z=-H$. The right-hand side forcing terms of (2.37)–(2.39) include Bragg scattering terms (III and IV), effects of spatial heterogeneities (I, II and V), non-stationarity (VI), and third-order nonlinear surface terms that are gathered here in the term NL_3. This set of equations is linear in ϕ_3. Therefore, ϕ_3 is the sum of a homogeneous solution (absorbed in ϕ_1) and four particular solutions,

$$\phi_3 = \phi_3^{\mathrm{sc}} + \phi_3^{\mathrm{he}} + \phi_3^{\mathrm{ns}} + \phi_3^{\mathrm{nl}}, \tag{2.40}$$

where sc, he, ns and nl, stand for scattering, heterogeneity, non-stationarity and nonlinarity, respectively. Each solution satisfies (2.37)–(2.39) forced, respectively, by the scattering terms (III and IV) only, the heterogeneity terms (I, II and V) only, the non-stationarity term (VI) only, and the surface nonlinearity terms (NL_3) only. Although ϕ_3^{nl} is resonantly forced, it contributes only bounded terms to E_4 (Hasselmann 1962). Similarly, nonlinear contributions to the scattering terms III and IV (the $O(\varepsilon^2\eta)$ products involving ϕ_2^{nl} and bottom undulations) yield only bounded contributions in E_4. The remaining solutions ϕ_3^{sc}, ϕ_3^{he} and ϕ_3^{ns} contribute growing terms, $E_{3,1}^{\mathrm{sc}}$, $E_{3,1}^{\mathrm{he}}$ and $E_{3,1}^{\mathrm{ns}}$, to E_4. Following the method used to obtain $\partial E_4^{2,2}/\partial t$, at $\tilde{\boldsymbol{x}} = \boldsymbol{0}$ we have (Appendices B, C and D)

$$\frac{\partial\left[E_{3,1}^{\mathrm{sc}}(\boldsymbol{k}) + E_{1,3}^{\mathrm{sc}}(\boldsymbol{k})\right]}{\partial t} = -K(k,H)\int_0^{2\pi} \cos^2(\theta-\theta') F^B(\boldsymbol{k}-\boldsymbol{k}') E_2(\boldsymbol{k})\,\mathrm{d}\theta', \tag{2.41}$$

$$\frac{\partial\left[E_{3,1}^{\mathrm{ns}}(\boldsymbol{k}) + E_{1,3}^{\mathrm{ns}}(\boldsymbol{k})\right]}{\partial t} = -\frac{\partial E_2(\boldsymbol{k})}{\partial t}, \tag{2.42}$$

$$\frac{\partial\left[E_{3,1}^{\mathrm{he}}(\boldsymbol{k}) + E_{1,3}^{\mathrm{he}}(\boldsymbol{k})\right]}{\partial t} = -\boldsymbol{C}_g(\boldsymbol{k})\cdot\nabla E_2(\boldsymbol{k}_r), \tag{2.43}$$

where $\boldsymbol{C}_g(\boldsymbol{k})$ is the group velocity of linear waves (equation (D 9)), and $E_2(\boldsymbol{k}_r)$ is a Lagrangian variable that describes energy evolution along the ray trajectory $[\boldsymbol{x}(\boldsymbol{k},\beta r), \boldsymbol{k}_r(\boldsymbol{k},\beta r)]$ of wave component $\boldsymbol{k}$, where r is the along-ray coordinate. $E_2(\boldsymbol{k}_r)$ is defined by

$$F_{1,1}^{\Phi}(\tilde{\boldsymbol{x}},\tilde{t},\boldsymbol{k}_r) = \lim_{|\Delta\boldsymbol{k}_r|\to 0} \frac{F_{1,1,\boldsymbol{k}}^{\Phi}(\tilde{\boldsymbol{x}},\tilde{t})}{\Delta k_{r,x}\Delta k_{r,y}}, \tag{2.44}$$

$$E_2(\tilde{\boldsymbol{x}},\tilde{t},\boldsymbol{k}_r) = k_r F_{1,1}^{\Phi}(\tilde{\boldsymbol{x}},\tilde{t},\boldsymbol{k}_r)\tanh(k_r H). \tag{2.45}$$

Note that the advection term $\boldsymbol{C}_g(\boldsymbol{k})\cdot\nabla E_2(\boldsymbol{k}_r)$ describes the divergence of the energy flux in Lagrangian coordinates, and thus incorporates refraction and shoaling effects. All other terms in (2.42)–(2.43) depend only on the energy at $\tilde{\boldsymbol{x}} = \boldsymbol{0}$ where the Lagrangian wavenumber $\boldsymbol{k}_r$ is equal to the Eulerian wavenumber $\boldsymbol{k}$, and $E_2(\boldsymbol{k}_r) = E_2(\boldsymbol{k})$.

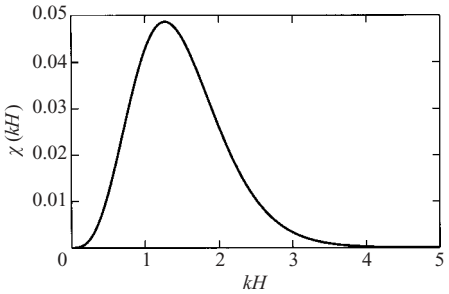

FIGURE 3. Values of $\chi(kH)$, as defined by (2.49).

2.5. *Energy balance*

Combining (2.35) and (2.41)–(2.43), the rate of change of the fourth-order spectrum (2.24) at $\tilde{\boldsymbol{x}} = \boldsymbol{0}$ is given by

$$\frac{\partial E_4(\boldsymbol{k})}{\partial t} = -\frac{\partial E_2(\boldsymbol{k})}{\partial t} - \boldsymbol{C}_g(\boldsymbol{k}) \cdot \nabla E_2(\boldsymbol{k}_r) + K(k,H) \int_0^{2\pi} \cos^2(\theta - \theta') F^B(\boldsymbol{k} - \boldsymbol{k}')[E_2(\boldsymbol{k}') - E_2(\boldsymbol{k})] \, \mathrm{d}\theta', \quad (2.46)$$

where $K(k,H)$ is given by (2.36).

To ensure that E_4 is bounded for large t, that is $\partial E_4/\partial t = O(\varepsilon)$, the right-hand side terms of (2.46) must balance. Recognizing the first two of these terms as the total derivative of $E_2(\boldsymbol{k}_r)$ along a ray trajectory, and replacing E_2 by E, we obtain (using dimensional and unscaled variables from now on) the Lagrangian energy balance equation at $\tilde{\boldsymbol{x}} = \boldsymbol{0}$

$$\frac{\mathrm{d}E(\boldsymbol{k}_r)}{\mathrm{d}t} = S_{\mathrm{Bragg}}(\boldsymbol{k}) + O(\varepsilon^5), \quad (2.47)$$

$$S_{\mathrm{Bragg}}(\boldsymbol{k}) = 4\pi g^{1/2} H^{-9/2} \chi(kH) \int_0^{2\pi} \cos^2(\theta - \theta') F^B(\boldsymbol{k} - \boldsymbol{k}')[E(\boldsymbol{k}') - E(\boldsymbol{k})] \, \mathrm{d}\theta', \quad (2.48)$$

with

$$\chi(kH) = \frac{(kH)^{9/2} \, [\tanh(kH)]^{1/2}}{\sinh(2kH) \, [2kH + \sinh(2kH)]}. \quad (2.49)$$

Equation (2.47) describes the net energy transfer at $\tilde{\boldsymbol{x}} = \boldsymbol{0}$ to a wave component with wavenumber $\boldsymbol{k}$ (propagating in direction θ), resulting from triad interactions involving a wave of the same radian frequency ω and a different wavenumber $\boldsymbol{k}'$ (direction θ'), and a bottom component with the difference wavenumber $\boldsymbol{l} = \boldsymbol{k} - \boldsymbol{k}'$ (figure 1). The energy transfer between components $\boldsymbol{k}$ and $\boldsymbol{k}'$ is proportional to the energy difference of the wave components and the bottom spectrum density at $\boldsymbol{l} = \boldsymbol{k} - \boldsymbol{k}'$. The factor $\cos^2(\theta - \theta')$ in (2.48) indicates that there is no energy transfer between waves propagating in perpendicular directions. The factor $\chi(kH)$ has a single maximum, approximately equal to 0.049 for the intermediate water depth $kH \approx 1.27$ (figure 3). In addition to directional and wavenumber dependencies, the scattering strength is proportional to $H^{-9/2}$, increasing strongly with decreasing water depth. Taking into account their different normalization of the bottom elevation spectrum, the present expression (2.48) of S_{Bragg} is 4 and 8 times smaller than the expressions given by Long (1973) and Hasselmann (1966), respectively.

2.6. *Conditions of validity*

The present theory is both a spectral generalization and higher-order energy conserving form of the solution given by Davies (1979) for sinusoidal bed undulations. Davies describes the generation of second-order waves ϕ_2, but uses constant amplitudes for ϕ_1, and thus does not account for the associated energy losses of the primary waves. In the present theory, the extension of the perturbation expansion to third-order provides the balancing terms $E_{1,3}$ and $E_{3,1}$ (equation (2.41)), necessary for the conservation of the total energy in (2.47). Whereas Davies' theory assumes small reflected wave amplitudes, (2.47) can describe finite cumulative reflections over large distances and even complete localization of waves over rough bottom topography. However, the present theory assumes that significant wave-amplitude variations occur over scales of $O(\alpha^{-1})$ wavelengths with $\alpha \approx \varepsilon^2$, and thus cannot accurately describe strong localized scattering that modifies the wave amplitudes over scales of only a few wavelengths (see Mei 1985 for a discussion of those effects over sinusoidal bottom topography, including, in particular, the importance of near-resonant interactions in that case).

It should be noted that the wavenumber spectrum $E(k) = \int_0^{2\pi} kE(\boldsymbol{k})\,\mathrm{d}\theta$ was assumed to be continuous in order to derive (2.47) in the limit of large times, removing the singularities for perfect resonance in (A 6), and reducing the bandwidth of important near-resonant interactions to a region of the spectrum where $E(\boldsymbol{k})$ can be considered constant. Thus, (2.47) is not valid for monochromatic waves. Whereas the initial growth of the scattered energy is proportional to t^2 for resonant monochromatic waves, it is only proportional to t for waves with a continuous spectrum, because resonance becomes more selective with time, affecting a wavenumber bandwidth that narrows proportionally to t^{-1}.

Another consequence of the asymptotic large time limit taken in Appendices A–D, is that the stochastic model (2.47) may not describe accurately wave evolution over natural seabeds which are often not homogeneous over scales of many wavelengths. The robustness of (2.47) for short propagation distances is examined in § 3 through comparisons with deterministic models for wave evolution over a finite patch of sinusoidal bars. Equation (2.47) includes wave–bottom interactions with $|\boldsymbol{k} - \boldsymbol{k}'| \ll k$, violating our scaling assumption $l \approx k$. This particular aspect is discussed in § 3.4.

2.7. *Extensions of the present theory*

The present energy balance (equation (2.47)) may be extended to higher orders of η and/or ε by closing the energy Taylor expansion at E_6, giving an evolution equation for $E_2 + E_4$. In the case of steeper waves, say $\alpha \approx \beta \approx \gamma \approx \eta^2 \approx \varepsilon^4$, it can be seen that all the energy transfer terms derived here (equations (2.35), (2.41)–(2.43)) are moved from E_4 to E_6, joining the additional source term S_{nl} that represents resonant quartet wave–wave interaction (Hasselmann 1962; Herterich & Hasselmann 1980). Extensions to steeper waves and steeper topography, for example $\alpha \approx \beta \approx \gamma \approx \eta^4 \approx \varepsilon^4$, should yield at least two additional source terms, corresponding to higher-order Bragg scattering (class II and III, see for example Liu & Yue 1998).

Furthermore, it can be expected that including higher-order heterogeneity effects and nonlinearity should introduce nonlinear effects on the left-hand side of (2.47), as described by Willebrand (1975). For example, in the present theory, E_6 contains correlations between the tertiary waves ϕ_3^{nl} and the heterogeneity and non-stationarity terms ϕ_3^{he} and ϕ_3^{ns}. Thus, it may be possible to derive a more complete energy balance equation with not only the source terms for the individual physical processes that

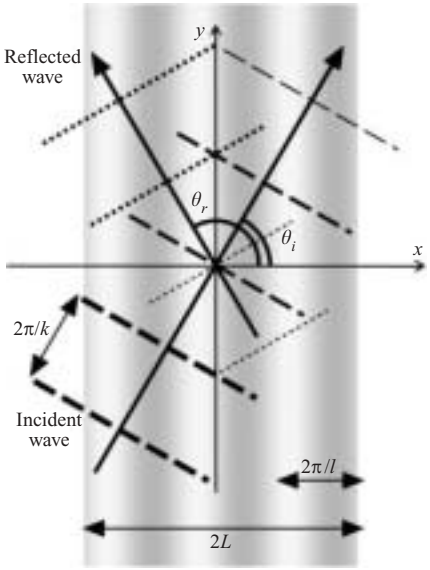

FIGURE 4. Schematic of incident waves (dashed crests) and reflected waves (dotted crests) on a patch of sinusoidal bars (grey shades).

contribute to the evolution of the wave spectrum, but also the cross-interactions of these processes that are usually neglected in wave prediction models (Komen *et al.* 1994).

3. Random waves over a finite patch of sinusoidal bars

Following Davies (1979), we consider a simple seabed consisting of sinusoidal bars on an otherwise flat bottom for which analytical results exist that have been verified in laboratory experiments. Waves arriving from $x = -\infty$ at an incidence angle θ_I are partially reflected, in a direction $\theta_R = \pi - \theta_I$ by a patch of m sinusoidal bars of amplitude b, aligned with the y-axis. The barred profile $h = b\sin(lx)$ covers the region $-L < x < L$ where $L = m\pi/l$ and l is the bar wavenumber (figure 4). The incident wave field is assumed to be a continuous spectrum $E_I(k)$ of unidirectional ($\theta = \theta_I$) waves. The total reflected energy E_R in the far field ($x \ll -L$) predicted by the stochastic and deterministic theories are compared for both normal and oblique incidence cases, in the limit of large m, corresponding to large propagation times for which (2.47) is valid, and for finite m.

3.1. *Stochastic source term approach*

In a steady state, uniform along the y-axis, the energy balance (2.47) for the bottom profile described above, simplifies to

$$C_g \cos\theta \frac{\mathrm{d}E(\boldsymbol{k})}{\mathrm{d}x} = S_{\mathrm{Bragg}}(\boldsymbol{k}). \tag{3.1}$$

In order to evaluate S_{Bragg} (equation (2.48)), we approximate the finite patch of sinusoidal bars as a subsection of a sinusoidal bottom extending to infinity, for which

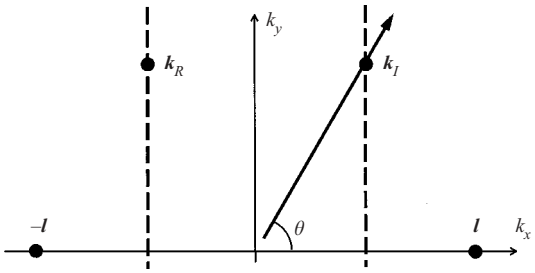

FIGURE 5. Resonant triads for waves over sinusoidal bars represented on the wavenumber plane. The bar wavenumbers are fixed at $(l, 0)$ and $(-l, 0)$ and all possible pairs of resonant surface wavenumbers $\boldsymbol{k}_I$ and $\boldsymbol{k}_R$ lie on the vertical dashed lines. For the wave direction θ shown here, the directional spectral density $E(\theta)$ (the integral of $kE(\boldsymbol{k})$ along the thick arrow) is affected by energy transfers in the resonant $(\boldsymbol{k}_I, \boldsymbol{k}_R, \boldsymbol{l})$ triad.

the bottom variance spectrum F^B is a double Dirac distribution

$$F^B(\boldsymbol{l}) = \tfrac{1}{4}b^2\,[\delta(l, 0) + \delta(-l, 0)]\,. \tag{3.2}$$

Outside the barred section ($|x| > L$), F^B is set equal to zero. The singularity in (3.2) is removed in S_{Bragg} by integrating (3.1) over k for a fixed direction θ (figure 5). Changing variables from (k, θ') to $(l_x, l_y) = k(\cos\theta - \cos\theta', \sin\theta - \sin\theta')$ (the corresponding resonant bottom wavenumber) we obtain

$$\frac{\mathrm{d}E(\theta)}{\mathrm{d}x} = \frac{8\pi}{\cos\theta}\iint_{\boldsymbol{k}\cdot\boldsymbol{l}>0}\frac{\cos^2(\theta-\theta')F_b(\boldsymbol{l})\,[E(\boldsymbol{k}-\boldsymbol{l}) - E(\boldsymbol{k})]\,k^5}{[1-\cos(\theta-\theta')]\,[2kH + \sinh(2kH)]^2}\,\mathrm{d}l_x\,\mathrm{d}l_y, \tag{3.3}$$

where

$$E(\theta) = \int_0^\infty kE(k\cos\theta, k\sin\theta)\,\mathrm{d}k \tag{3.4}$$

is the directional spectrum integrated over all wavenumbers, and the Jacobian $J = 1/\{k[1-\cos(\theta-\theta')]\}$ of the transform from (k, θ') to (l_x, l_y) is used. Note that the integration over $\boldsymbol{l}$ is restricted to the half-plane where $\boldsymbol{k}\cdot\boldsymbol{l} > 0$ (figure 5).

For $-\frac{1}{2}\pi < \theta < \frac{1}{2}\pi$ (3.3) describes the evolution of an incident component with direction $\theta_I = \theta$. Only interactions in the neighbourhood of the resonant triad $\boldsymbol{k}_I = \frac{1}{2}l(1, \tan\theta)$, $\boldsymbol{k}_R = \frac{1}{2}l(-1, \tan\theta)$, $\boldsymbol{l} = (l, 0)$ contribute to this integral (figure 5). For $\frac{1}{2}\pi < \theta < \frac{3}{2}\pi$, (3.3) describes the evolution of a reflected component with direction $\theta_R = \theta$ resulting from the resonance of $\boldsymbol{k}_I = \frac{1}{2}l(1, -\tan\theta)$, $\boldsymbol{k}_R = \frac{1}{2}l(-1, -\tan\theta)$, $\boldsymbol{l} = (-l, 0)$. Substitution of (3.2) in (3.3) yields

$$\frac{\mathrm{d}E_R}{\mathrm{d}x} = -D_x[E(\boldsymbol{k}_I) - E(\boldsymbol{k}_R)] \quad \text{for} \quad -L < x < L, \tag{3.5}$$

where

$$D_x = \frac{\pi b^2\cos^2(2\theta_I)l^5}{16\cos^6\theta_I\,[1+\cos(2\theta_I)]\,\left[lH/\cos\theta_I + \sinh(lH/\cos\theta_I)\right]^2}. \tag{3.6}$$

For weak reflection ($E(\boldsymbol{k}_I) \gg E(\boldsymbol{k}_R)$), we can neglect changes in $E(\boldsymbol{k}_I)$. Integrating (3.5) from L to $-L$ yields

$$E_R = 2LD_xE(\boldsymbol{k}_I) \quad \text{for} \quad x < -L. \tag{3.7}$$

For unidirectional incident waves with a spectrum $E_I(\boldsymbol{k}) = \delta(\theta-\theta_I)E_I(k)/k$, the total

reflected energy is given by

$$E_R = D l E_I(k_I), \tag{3.8}$$

where D is a non-dimensional coefficient

$$D = \frac{2LD_x}{lk_I} = \frac{m\pi^2 b^2 \cos^2(2\theta_I) l^2}{4\cos^5\theta_I\,[1+\cos(2\theta_I)]\left[lH/\cos\theta_I + \sinh(lH/\cos\theta_I)\right]^2}. \tag{3.9}$$

For the particular case of normal incidence ($\theta_I = 0$) D reduces to

$$D = \frac{m\pi^2 b^2 l^2}{8\,[lH + \sinh(lH)]^2}. \tag{3.10}$$

3.2. *Comparison with deterministic theory for normal incidence*

In Davies' (1979) theory for weak reflection of a normally incident monochromatic wavetrain by a patch of m sinusoidal bars with amplitude b, the ratio of the reflected and incident wave amplitudes is given by

$$\kappa_{\mathrm{DH}} = \frac{2bk}{2kH + \sinh(2kH)} \frac{(-1)^m 2k}{l} \frac{\sin(2kL)}{(2k/l)^2 - 1}. \tag{3.11}$$

Theoretical values of κ_{DH} have been verified experimentally by Heathershaw (1982; see also Davies & Heathershaw 1984), even in cases with large reflection coefficients.

For random waves with a wavenumber spectrum $E_I(k)$, the reflected energy $E_{R,\mathrm{DH}}$ is therefore the convolution of $|\kappa_{\mathrm{DH}}(k)|^2$ and $E_I(k)$,

$$E_{R,\mathrm{DH}} = \int_0^\infty |\kappa_{\mathrm{DH}}(k)|^2 E_I(k)\,\mathrm{d}k. \tag{3.12}$$

The response function $|\kappa_{\mathrm{DH}}|^2$ has a 'resonant lobe' of width π/L and height proportional to m^2 centred at the resonant wavenumber $k = \frac{1}{2}l$, and narrower side lobes at higher and lower wavenumbers (figure 6, dotted curve). In the limit of large m (equivalent to the large t limit in the stochastic theory), $|\kappa_{\mathrm{DH}}|^2$ approaches a Dirac distribution

$$|\kappa_{\mathrm{DH}}|^2 \sim \frac{m\pi^2 l}{8} \left(\frac{2bk}{2kH + \sinh(2kH)}\right)^2 \left(\frac{2k}{l}\right)^2 \delta\left(\frac{l}{2}\right). \tag{3.13}$$

Since $E_I(k)$ is continuous, the substitution of (3.13) in (3.12), yields

$$E_{R,\mathrm{DH}} \sim \frac{m\pi^2 b^2 l^3}{8\,[lH + \sinh(lH)]^2} E_I\left(\frac{l}{2}\right), \tag{3.14}$$

which is identical to the stochastic theory prediction (equations (3.8) and (3.10)). The exact agreement of the stochastic and (experimentally verified) deterministic theories in the limit of large m, where both are valid, confirms that the coupling factor χ (equation (2.49)), which differs by factors of 8 and 4 from previous publications (Hasselmann 1966; Long 1973), is correct.

3.3. *Oblique incidence and finite numbers of bars*

Davies' (1979) theory for wave reflection from sinusoidal bars was generalized to oblique incidence and finite reflection coefficients by Mei (1985), using an approximation for weak detuning from resonance. Dalrymple & Kirby (1986) applied Mei's theory to a finite patch of bars and derived the amplitude reflection coefficient κ_{DK} (their equations 5 and 9). For normal incidence, κ_{DK} is in good agreement with the

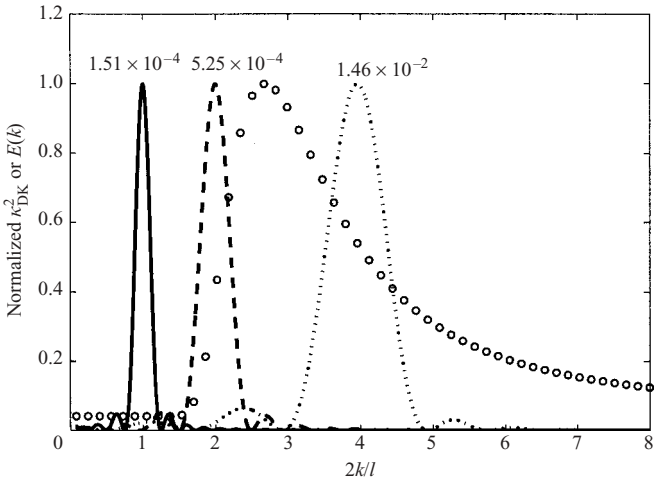

FIGURE 6. Response function $|\kappa_{DK}|^2$ for $H = 25$ m, $2\pi/l = 300$ m, $b = 0.05$ m, $m = 4$, and three incidence directions: ——, $\theta_i = 0$; – – –, $\theta_i = 60°$; · · ·, $\theta_i = 75.5°$ (corresponding to resonant wavenumbers $k = \frac{1}{2}l$, $k = l$ and $k = 2l$). The response functions are normalized by their maximum values indicated on the figure. For reference, a generic wave spectrum is included (○, arbitrary units) with a Pierson–Moskowitz shape, a peak period of 14 s, and uniform infragravity energy levels. The total reflected energy is the convolution of $|\kappa_{DK}|^2$ and the wave spectrum.

experimental results of Davies & Heathershaw (1984), and reduces to κ_{DH} in the limit of small bar amplitude b. For oblique incidence, no experimental verification exists, but Mei's theory was verified numerically with solutions of Kirby's generalized mild slope equations (Kirby 1993). Values of $|\kappa_{DK}|^2$ for a patch of four bars of wavelength $2\pi/l = 300$ m, and amplitude $b = 0.05$ m in 25 m depth, are shown in figure 6 as a function of k/l for different incidence angles θ_I. The interaction between the bottom undulations and the surface gravity waves is dominated by near-resonant triads, for which $|\kappa_{DK}|^2$ is maximum. The Bragg resonance condition $k = 2l/\cos\theta_I$ determines the wavenumber for which reflection is maximum, as a function of the incidence angle. For example, for the wave spectrum shown in figure 6, back scattering ($\theta_I \approx 0$, $\theta_R \approx 180°$) is confined to the long wavelength (infragravity) part of the spectrum, and shorter swells are scattered forward (see the response functions for $\theta_I = 60°$, $\theta_R = 120°$ and $\theta_I = 75.5°$, $\theta_R \approx 104.5°$ in figure 6).

To determine the accuracy of the stochastic theory for a finite patch of bars, the total reflected energy E_R predicted by (3.8)–(3.9), valid only in the limit of large m, is compared to the 'exact' $E_{R,DK}$ predicted by the deterministic theory (equation (3.12) where κ_{DH} is replaced by κ_{DK}), valid for arbitrary m. In these calculations, $E_I(k)$ is taken to be a Pierson–Moskowitz spectrum (Pierson & Moskowitz 1964) with a peak period $T_p = 14$ s. A white background spectrum $E(k) = 0.04E_I(k_p)$ is added to represent contributions of longer wavelength infragravity waves (figure 6). The convolution integral (3.12) is computed numerically over the range $0.005 < k/l < 4$, for incidence angles $\theta_I = 0°$, 60° and 75.5°. Other parameters are $H = 25$ m and $b = 0.05$ m. A small b value was chosen to have a small reflection coefficient ($\kappa_{DK} < 0.1$) because (3.8) neglects variations in the incident energy E_I and thus is valid only for weak reflections. The relative difference between stochastic and deterministic theories is shown in figure 7 as a function of m. The difference is sensitive to the variations of the wave spectrum across the resonant lobe and the relative magnitude of the

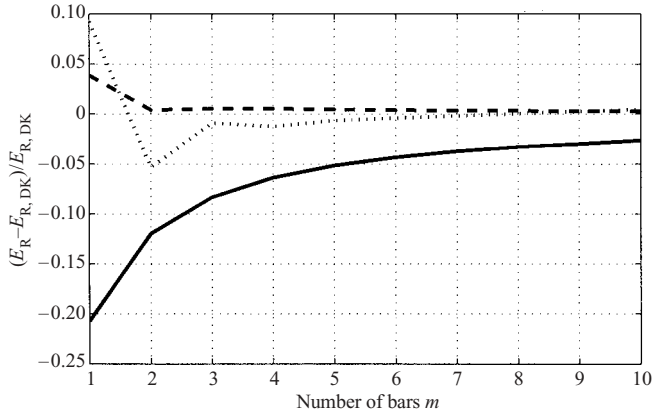

FIGURE 7. Relative differences between the reflected energy predicted by the stochastic theory (equation (3.8)) and the spectral form (equation (3.12), replacing κ_{DH} by κ_{DK}) of Dalrymple and Kirby's theory, as a function of the number of bars m. All other parameters are the same as in figure 6. The incident wave spectrum is shown in figure 6.

side-lobes of the response function $|\kappa_{DK}|^2$, these effects vanish in the limit $m \to \infty$ as the width of the resonant lobe and the height of the side-lobes go to zero. As m increases, the predictions of both theories converge, as expected since both theories are valid for large m. For all three incidence angles $\theta_I = 0°$, $60°$ and $75.5°$, the difference in wave energy reflections predicted by the stochastic and deterministic theories is less than 10% for more than three bars. This rapid convergence not only provides a further consistency check on the coupling factor χ (equation (2.49)) for cases of oblique incidence, but also indicates that the stochastic Bragg scattering theory is surprisingly robust, although formally valid only in the asymptotic limit of many bottom wavelengths, and yields reasonable estimates of energy transfers resulting from scattering by only a few bottom undulations.

3.4. *Bottom slope effects*

The large time limit used to evaluate fourth-order energy terms in Appendices A–D requires implicitly that the large-scale bottom slope does not significantly change the interaction over a distance Δr that allows waves to propagate across a sufficiently large number of bars m_a to approach the asymptotic limit of the energy transfer (figure 7). Wave refraction by the large-scale bottom slope changes the surface wavenumbers and thus introduces a detuning of near-resonant wave–bottom interactions. This detuning effect can be neglected only if changes in the surface wavenumbers are small compared to the width of the resonant lobe of the response function $|\kappa_{DK}|^2$ (figure 6).

For simplicity we consider a finite patch of m_a sinusoidal bars aligned with the y-axis, with wavenumber l, superimposed on a plane bottom with a downward slope β in a direction θ_b. The along-ray gradient of the resonance mismatch $u = (2k\cos\theta - l)/l$ is given by

$$\frac{\partial u}{\partial r} = \frac{2}{l}\left(\cos\theta\frac{\partial k}{\partial r} - k\sin\theta\frac{\partial \theta}{\partial r}\right). \tag{3.15}$$

Using Snel's law we have

$$\frac{\partial u}{\partial r} = \frac{-4\beta k^2\cos\theta_b}{l\,[2kH + \sinh(2kH)]}. \tag{3.16}$$

For small bottom slopes, the distance travelled by the waves across the bar field is $\Delta r \approx 2m_a\pi/(l\cos\theta)$, giving a change in the resonance mismatch

$$\Delta u \approx -\frac{2\pi m_a \beta \cos\theta_b}{\cos^3\theta\,[2kH + \sinh(2kH)]}. \tag{3.17}$$

Detuning of resonant interactions by refraction can be neglected if $|\Delta u|$ is small compared with the (normalized) width of the resonant lobe $1/m_a$, that is

$$m_a\,|\Delta u| \ll 1. \tag{3.18}$$

Equation (3.18) also follows from considering the phase difference between waves reflected by the first and m_ath bars, which should be small compared to $\frac{1}{2}\pi$ to allow the constructive interference that causes resonance.

Equation (3.18) is a necessary condition for the application of the stochastic theory. For a given bottom slope β, (3.18) imposes a maximum incidence angle $\theta_{\max}$. For practical purposes, we assume that the largest acceptable value of $m_a\,|\Delta u|$ is about 0.5, giving

$$\cos^3\theta_{\max} > \frac{4\pi m_a^2 \beta \cos\theta_b}{2kH + \sinh(2kH)}. \tag{3.19}$$

For example, considering 14 s period waves in 25 m depth with a bottom slope $\beta = 2\times10^{-4}$ at an angle $\theta_b = 60^\circ$, and taking $m_a = 2$, the source term (2.48) is expected to overestimate significantly the energy of scattered waves for incidence angles greater than $\theta_{\max} \approx 83^\circ$, corresponding to a ratio $k/l = 4.3$.

It should be noted that (3.18) is consistent with the scaling of (2.1)–(2.4) requiring that bottom and surface elevations have comparable horizontal scales. This scaling is violated for large-angle interactions (i.e. $k \gg l$ for θ close to 90°), even on a flat bottom. In the following, the contribution of wave–bottom interactions to (2.48) is taken to be accurate for $\theta < \theta_{\max}$ and is neglected for $\theta > \theta_{\max}$. This crude truncation of the interactions is expected to give only qualitative results for the scattering of waves at large incidence angles. Sensitivity of predicted spectral evolution to the choice of the cutoff angle $\theta_{\max}$ is examined for natural shelf topography in § 4.

4. Hindcast of wave scattering on a natural shelf

The effect of Bragg scattering on directional wave spectra evolution is illustrated here with a numerical model hindcast of swell evolution observed across the North Carolina shelf. The scattering source term S_{Bragg} (equation (2.48)) was implemented in the spectral model CREST (Ardhuin *et al.* 2001), that solves the energy balance (equation (2.47)) using a hybrid Eulerian–Lagrangian numerical scheme. In addition to S_{Bragg}, a bottom friction source term S_{fric} is included in the energy balance to account for energy dissipation in the boundary layer over a sandy movable bottom. Details of the model formulation, numerical scheme, treatment of boundary conditions, and parameterization of bottom friction are given in Ardhuin *et al.* (2001). S_{Bragg} is evaluated using bottom elevation spectra that were estimated from high-resolution bathymetry surveys. Processes not represented in the model such as wind–wave generation, effects of currents, wave breaking, and nonlinear effects, are expected to be negligible because at the time of the hindcast (21:00 Greenwich Mean Time, 20 October 1994) local wind speeds ($3\,\text{m s}^{-1}$), and current velocities ($\approx 20\,\text{cm s}^{-1}$, Lentz *et al.* 1999) were weak, and the observed waves were long-period (≈ 13 s) swell with low significant height (≈ 1 m).

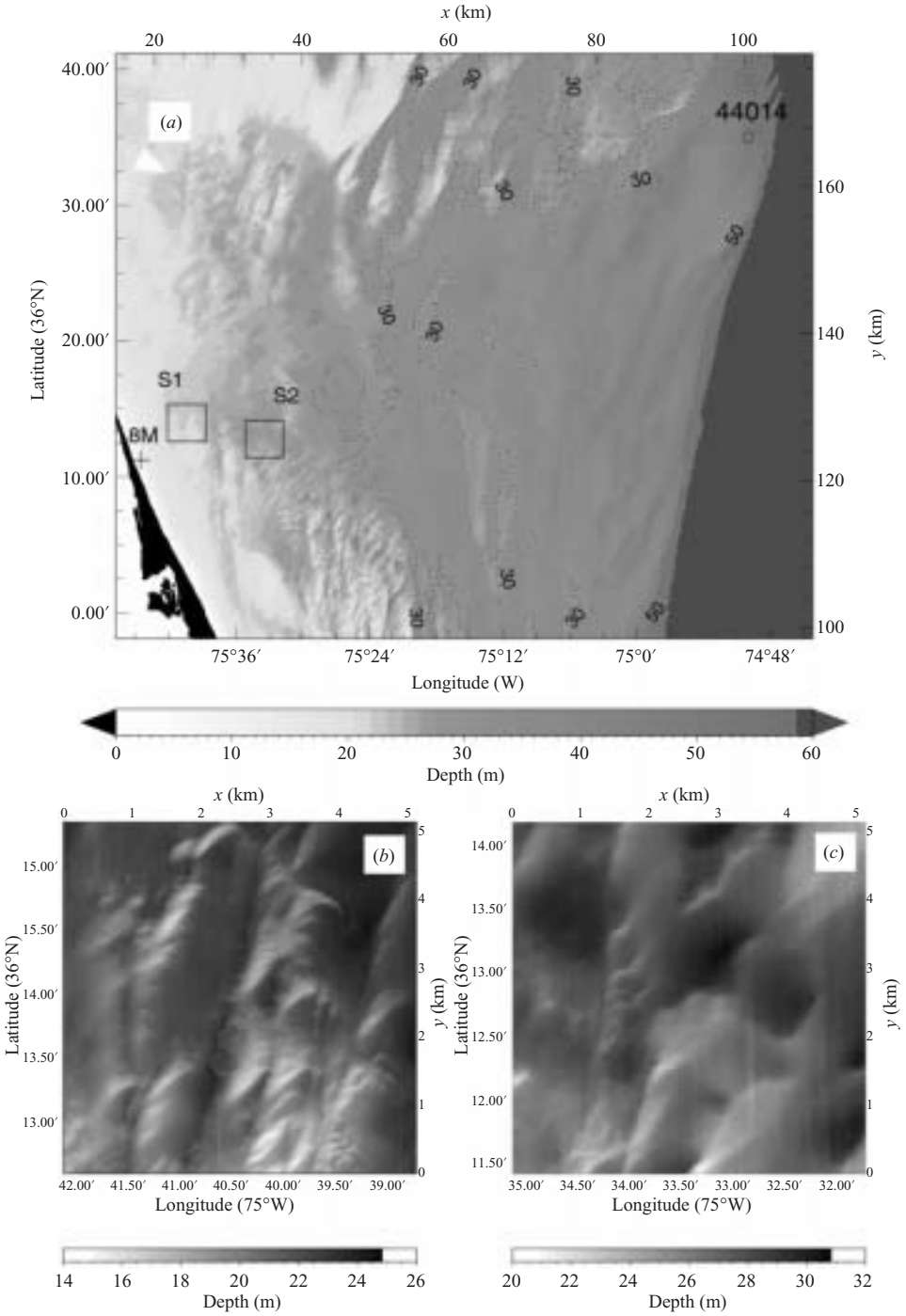

FIGURE 8. (*a*) Bottom topography of the North Carolina continental shelf. The squares marked S1 and S2 are the regions enlarged in (*b*, *c*). Other symbols indicate locations of the FRF 8 m depth array (8M) and NDBC 3 m discus buoy (44014).

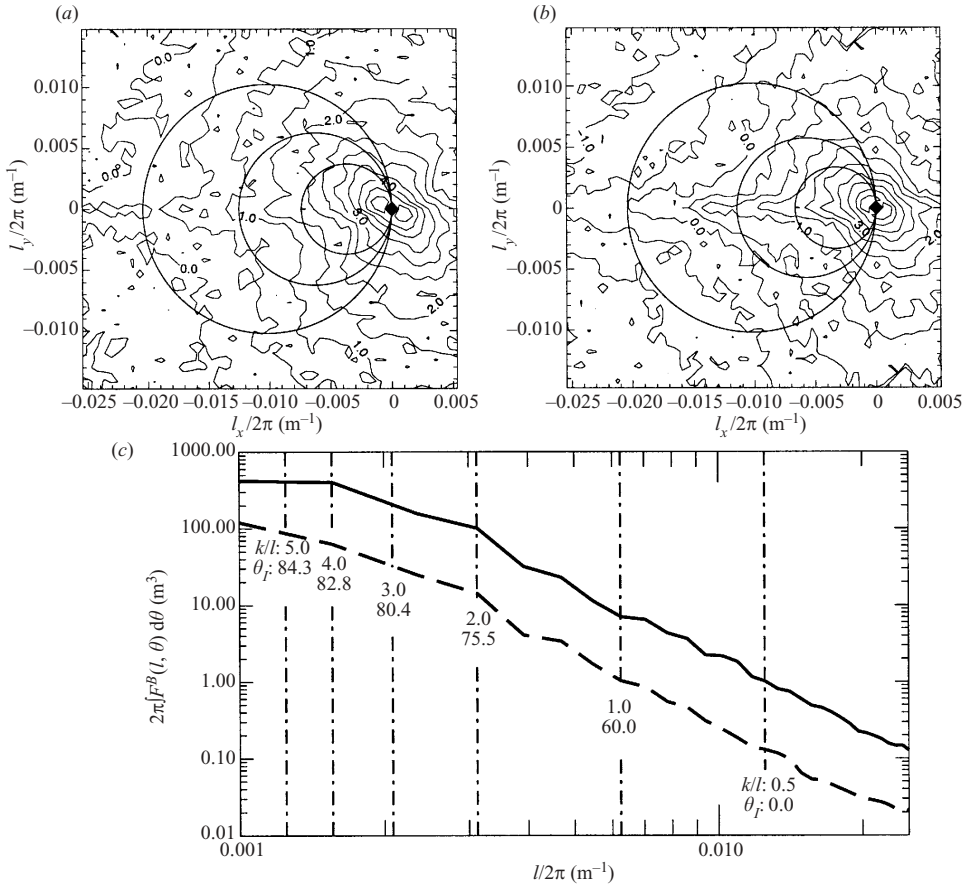

FIGURE 9. Contour plots of the bottom variance spectra estimates for regions (*a*) S1 and (*b*) S2. The contour values are $\log_{10}(4\pi^2 F^B)$ with F^B in m^4 rad^{-2}, and the contour interval is 0.5. Circles indicate the bottom components that interact with waves arriving from the east with frequencies 0.05 (inner circle), 0.12 (middle circle) and 0.25 Hz (outer circle). Axes units are reciprocal wavelengths $l_x/(2\pi)$ and $l_y/(2\pi)$. (*c*) Direction-integrated spectra for —, S1; - - -, S2. The vertical lines indicate the bottom scales responsible for scattering 0.08 Hz swell, for various incidence angles θ_I.

4.1. *Wave data*

Frequency-directional wave spectra were estimated from measurements on the outer and inner shelf near Duck, North Carolina (figure 8*a*). An array of pressure sensors, located 1 km from the shoreline in 8 m depth, was operated by the Army Corps of Engineers Field Research Facility (FRF), in Duck, North Carolina, and a 3 m discus pitch and roll buoy located close to the shelf break, in 49 m depth, was operated by the National Data Buoy Center (NDBC). Standard techniques (Herbers, Elgar & Guza 1999; Ardhuin *et al.* 2001) were used to obtain estimates of the frequency-directional wave spectra at both locations. The NDBC buoy wave spectrum was transformed across the shelf break to deep water using Snel's law, assuming parallel depth contours, in order to obtain the offshore boundary condition for the model.

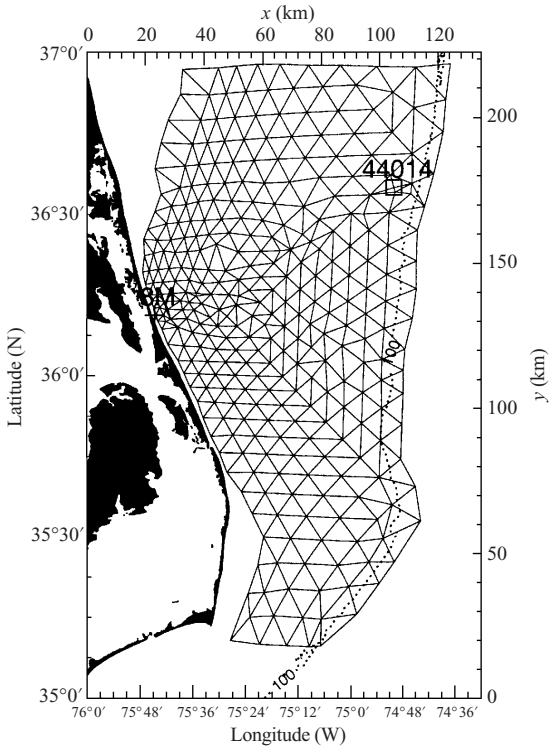

FIGURE 10. Model grid. The grid points where the source term is evaluated are the nodes of the triangular mesh. A linear interpolation is applied in each triangle to approximate the source term along the rays. The 100 m depth contour is indicated by the dotted line.

4.2. *Bottom topography*

Bathymetric data for most of the shelf was available from the National Ocean Service (NOS). In regions not covered by the NOS archives, water depths were measured during instrument deployment and recovery cruises in a series of experiments (DUCK94; Sandy Duck; SHOWEX) on the North Carolina continental shelf, using a single precision depth recorder. Additionally, high-resolution multibeam sonar bathymetric surveys were conducted during the SHOWEX experiment in November and December 1999, in two $6 \times 6\,\mathrm{km}^2$ regions of the inner shelf (labelled S_1 and S_2 in figure 8*a*). This data set was processed with the MB-System software (Caress & Chayes 1995) to obtain 10 m resolution grids shown in figure 8(*b*, *c*). The vessel motion and tide were carefully removed, although a slight but systematic measurement bias is still noticeable in the striped pattern of figure 8(*c*), yielding an artificial ridge of spectral densities on the *x*-axis of figure 9(*b*). Although the high-resolution bathymetry data were acquired five years after the wave data, comparisons with depth soundings, performed within a few months of the wave data collection, show good agreement, suggesting that bottom topographic features of scales larger than 500 m have not moved in regions S_1 and S_2.

Bottom elevation spectra $F_1^B(\boldsymbol{l})$ and $F_2^B(\boldsymbol{l})$ (figure 9*a*, *b*) were estimated for regions S_1 and S_2, respectively, based on bidimensional Fourier transforms of Hanning windowed $1.6 \times 1.6\,\mathrm{km}^2$ segments with 50% overlap. The large-scale bottom slope was previously

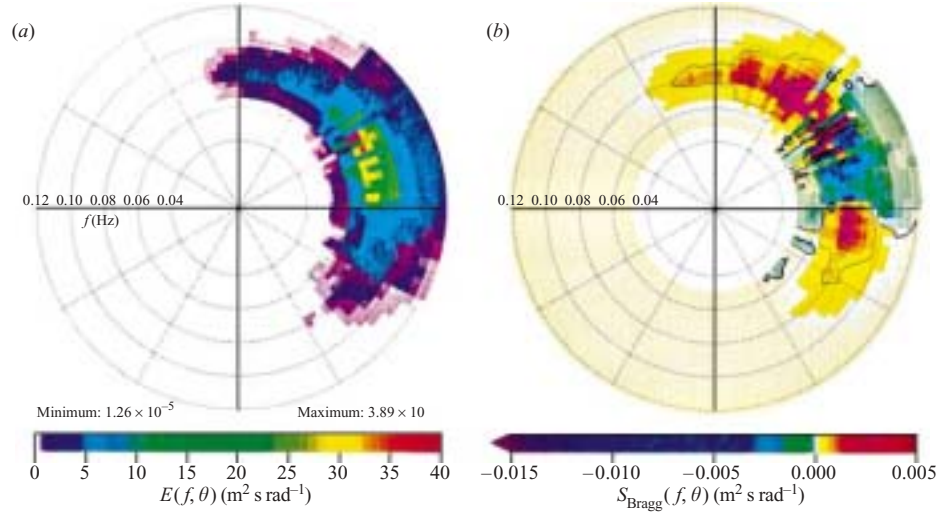

FIGURE 11. (*a*) Predicted wave spectrum E in region S_1 (figure 8) and (*b*) corresponding Bragg scattering source term S_{Bragg}, based on bottom spectrum F_1^B. Contours in (*b*) are solid for positive values (yellow to red colour shades), solid and thick for zero, and dashed for negative values (green to blue colour shades). $H_s = 0.92\,\mathrm{m}$; $f_p = 0.078\,\mathrm{Hz}$; mean direction at $f_p = 69.5°$; spread at $f_p = 24.00°$.

removed from each segment using a bilinear fit. Spectra of the large-scale shelf topography (not shown), computed from the entire bathymetry grid, are consistent with the spectral levels at small l shown in figure 9(*a*, *b*). The bottom elevation spectra are not isotropic, showing a preferential north-east/south-west orientation of intermediate scale features (200–1000 m) that are most important for swell scattering. It also appears that bottom spectral levels at these scales are about a factor 4 higher in region S_1 (15–25 m water depth, variance $1.4\,\mathrm{m}^2$) than in the deeper region S_2 (20–40 m, variance $0.35\,\mathrm{m}^2$, see figure 9*c*). As we lack detailed topographic information in other regions, the bottom elevation spectrum used in model hindcasts is taken to be uniform over the entire continental shelf. Hindcasts are presented in § 4.4 based on both estimates $F_1^B(\boldsymbol{l})$ and $F_2^B(\boldsymbol{l})$, illustrating the likely range of scattering effects.

4.3. *Numerical model*

The numerical wave model CREST used for the present calculations is described by Ardhuin *et al.* (2001). The model consists of a precomputation of wave rays and a Lagrangian time integration scheme for the energy balance (equation (2.47)). In contrast to more widely used finite-difference schemes (see for example the WAMDI group 1988; Booij, Ris & Holthuijsen 1999), the Lagrangian approach avoids numerical diffusion that could cause an artificial broadening of the wave spectrum in shallow water (not related to physical scattering processes). The Eulerian model grid, shown in figure 10 is unstructured and much coarser than the bathymetry grid. It consists of 329 points distributed over a large portion of the shelf between latitudes 35° and 37° N. Wave rays are traced backwards from the Eulerian grid points to the model boundary, using a smoothed (2 km scale) bathymetry grid that resolves wave refraction over the large-scale shelf topography. Along each ray, the energy balance (equation (2.47)) is integrated in time. At the grid points, the full wave spectrum $E(\boldsymbol{k})$ is evaluated using ensemble averages of rays within finite wavenumber bands $\boldsymbol{k}_{q,i}$

corresponding to 19 frequency bands f_q spaced exponentially with a 5% increment from 0.05 Hz to 0.12 Hz, and 120 direction bands θ_i spaced linearly over a full circle with a 3° resolution. The spectral source terms $S_{\rm fric}(\boldsymbol{k})$, representing bottom friction (Ardhuin *et al.* 2001, equation 13), and $S_{\rm Bragg}(\boldsymbol{k})$, given by (2.48), are evaluated at the grid points based on the local spectrum $E(\boldsymbol{k})$ and other parameters. $S_{\rm fric}(\boldsymbol{k})$ and $S_{\rm Bragg}(\boldsymbol{k})$ are interpolated onto the ray trajectories to account for the energy losses (bottom friction), and exchanges with other wave components (scattering), of component $\boldsymbol{k}$ during propagation. Details of the time integration and interpolation schemes can be found in Ardhuin *et al.* (2001).

The model was run here with constant offshore boundary conditions and a fixed integration time step $\Delta t = 10$ min, until a steady state was reached. To determine accurately the contribution of $S_{\rm Bragg}$ over the time step Δt, an implicit integration scheme was used. Omitting other source terms and propagation effects, (2.47) can be written in discretized form and for a given wavenumber magnitude k, as a set of linear equations

$$\frac{\partial E(k,\theta_i)}{\partial t} = 4\pi g^{1/2} H^{9/2} \chi(kH) \sum_j L_{i,j}(k) E(k,\theta_j) \quad \text{for all } i, \tag{4.1}$$

where θ_i are the discretized directions with $\boldsymbol{k}_i = k(\cos\theta_i, \sin\theta_i)$ and the matrix $\mathbf{L}(k)$ is given by

$$L_{i,j}(k) = \left[\cos^2(\theta_i - \theta_j) F^B(\boldsymbol{k}_i - \boldsymbol{k}_j) - \delta_{ij} \sum_n \cos^2(\theta_i - \theta_n) F^B(\boldsymbol{k}_i - \boldsymbol{k}_n) \right] \Delta\theta, \tag{4.2}$$

with $\delta_{ij} = 1$ for $i = j$, and 0 otherwise. As discussed in § 3.4, $F^B(\boldsymbol{l})$ is replaced by zero in (4.2) for k/l greater than $(k/l)_{\max}$. Since $\mathbf{L}$ is real and symmetric, it can be diagonalized and represented as the matrix product $\mathbf{L} = \mathbf{V}\mathbf{D}\mathbf{V}^T$ where $\mathbf{D}$ is a diagonal matrix with the eigenvalues λ_i as diagonal elements, the columns of $\mathbf{V}$ are the corresponding normalized eigenvectors, and $\mathbf{V}^T$ is the transpose of $\mathbf{V}$. Using this decomposition the solution of (4.1) can be given in the form

$$E(k,\theta_i,t+\Delta t) = \sum_j \sum_l V_{i,j}(k) \exp\left[4\pi g^{1/2} H^{-9/2} \chi(kH) \lambda_j(k) \Delta t\right] V_{l,j}(k) E(k,\theta_l,t). \tag{4.3}$$

The source term $S_{\rm Bragg}$ (R in (12) of Ardhuin *et al.* 2001) is given by the average change in $E(k,\theta_i,t)$ over a time step Δt

$$S_{\rm Bragg}(k,\theta_i) = [E(k,\theta_i,t+\Delta t) - E(k,\theta_i,t)]/\Delta t. \tag{4.4}$$

The matrices $\mathbf{V}(k)$ and eigenvalues $\lambda_i(k)$ are precomputed using Jacobi's algorithm (see for example Press *et al.* 1992) for 500 values of k covering the entire range of wavenumbers in the model, and the resulting matrices $\mathbf{V}$ and $\mathbf{D}$ are interpolated on the spectral model grid. The high accuracy of the implicit numerical scheme was confirmed through comparisons with an explicit fifth-order Cash–Karp Runge–Kutta method.

4.4. *Hindcast*

The model hindcast was performed both with and without the Bragg scattering source term to isolate the scattering effects from other processes (refraction, shoaling and bottom friction), using two different measured bottom elevation spectra ($F_1^B(\boldsymbol{l})$ and $F_2^B(\boldsymbol{l})$, figure 9) to estimate the possible variability of the scattering effects. Bottom components with wavelengths larger than 5 times the surface wavelength ($k/l > 5$)

are excluded in the evaluation of S_{Bragg} because, as discussed in § 3.4, the theory is not expected to be accurate for near-grazing angle interactions. Figure 11 shows an example wave spectrum predicted in region S_1 (20 m depth, figure 8), and the corresponding Bragg scattering source term. The source term has a 3-lobe shape with negative values near the peak θ_p of the directional wave spectrum, and positive maxima on both sides of the peak, at about $\theta_p \pm 30^\circ$. The interactions broaden the peak of the directional wave spectrum (forward-scattering) and cause weak, almost isotropic back-scattering. Sign reversals of S_{Bragg} within the main lobe (figure 11*b*) are caused by irregularities in the wave spectrum (figure 11*a*). Bragg scattering tends to smooth the directional wave spectrum, with an evolution time scale E/S_{Bragg} of the order of 10^3 and 10^4 s in 20 and 50 m depth, respectively.

The combined effect of Bragg scattering and refraction is shown in figure 12 with the predicted cross-shore evolution of the mean wave direction (from) at the peak frequency, $\bar{\theta}$, taken as the direction of the first-order moment vector

$$(a_1, b_1) = \int_0^{\pi} (\cos\theta, \sin\theta) E(f_p, \theta)\, \mathrm{d}\theta, \tag{4.5}$$

and the directional spread, in radians,

$$\sigma_\theta = \{2[1 - (a_1 \cos\bar{\theta} + b_1 \sin\bar{\theta})/E(f_p)]\}^{1/2}. \tag{4.6}$$

σ_θ ranges from 0° for unidirectional waves, to 81° for isotropic waves. Offshore propagating waves ($\pi < \theta < 2\pi$) are excluded in the analysis because the predicted back-scattering is weak, and reflection from the beach (Elgar, Herbers & Guza 1994), not represented in the model, is apparent in the 8 m data (figure 12*b*).

The model without Bragg scattering predicts the expected turning of $\bar{\theta}$ towards the shore-normal direction, caused by refraction (figure 12*a*). The introduction of Bragg scattering shifts the mean wave direction by an additional 1° to 10° to the north, because the bottom spectrum is not isotropic (figure 9). This effect is strongest for the hindcast which uses the bottom spectrum F_1^B with a larger variance. This small shift is not evident in the observations, suggesting that either the orientation of the bathymetric features in figure 9(*a*) may not be representative of other parts of the shelf, or other processes, not represented in the model, may be important. The detailed directional spectra, shown in figure 13, demonstrate that rather than shifting the entire spectrum, Bragg scattering skews the directional spectrum to the north (figure 13*c*, *d*) by preferentially scattering waves that propagate in directions parallel to the crests of the larger bedforms (i.e. waves from the north-east, figures 8 and 9).

Bragg scattering strongly affects the directional spread, causing a gradual increase of σ_θ across the shelf (figure 12*a*), that partly balances the reduction of the directional spread of the incident waves caused by refraction. Results based on bottom elevation spectra F_1^B and F_2^B are qualitatively similar, but the increase in directional spread is much larger for the more 'energetic' bottom spectrum F_1^B (a factor of about 2.5) than predicted for F_2^B (a factor 1.6). On the inner shelf, in 8 m depth, the observed σ_θ value of 14° is a factor 2 larger than the model prediction without Bragg scattering (7°, figure 12*b*), but falls in the range of model results with the source term S_{Bragg} based on bottom spectra F_1^B (18°) and F_2^B (12°).

The cutoff value $(k/l)_{\max}$ of the ratio between surface and bottom wavenumbers was varied from 0.5 (no scattering) to 5, in order to examine the importance of different bottom topography scales in the scattering process (figure 14). Increasing $(k/l)_{\max}$ from 0.5 (no scattering) to 1 (maximum scattering angle $\theta_{\max} = 60^\circ$) does not change significantly the directional properties of the waves. These interactions, involving

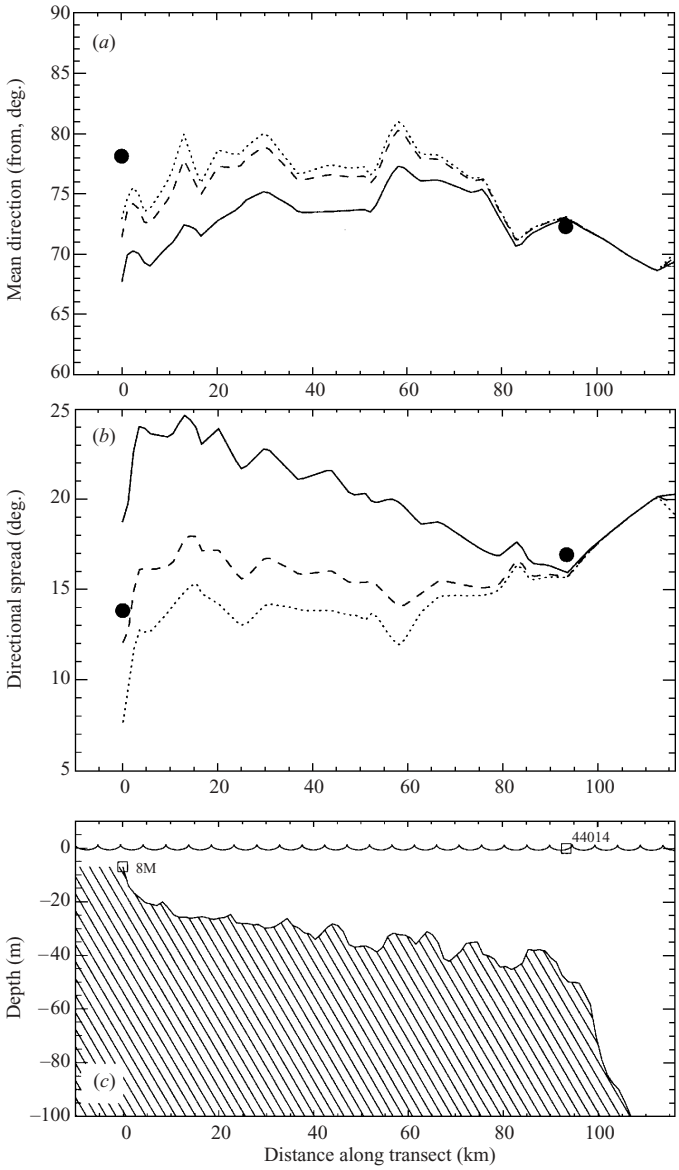

FIGURE 12. Measured (●) and predicted (—, with Bragg scattering using $F_1^B(\boldsymbol{I})$; - - -, with Bragg scattering using $F_2^B(\boldsymbol{I})$; ···, without Bragg scattering) variations of (*a*) $\bar{\theta}$ and (*b*) σ_θ at the peak frequency f_p. Results are shown for 20 October 2000, at 21:00 GMT, along a cross-shelf transect (*c*) extending from the 8 m depth array to deep water offshore of NDBC buoy 44014. A maximum value of $k/l = 5$ was used in the scattering calculations.

bottom components with wavelengths smaller than the surface wavelength, are weak because of the sharp roll-off of the bottom spectral levels at high wavenumbers. At the other end of the spectrum, results for $(k/l)_{\max}$ values of 4 and 5 are nearly identical, indicating that larger bottom features also do not significantly affect directional properties. Although the bottom spectral levels are relatively high at these small

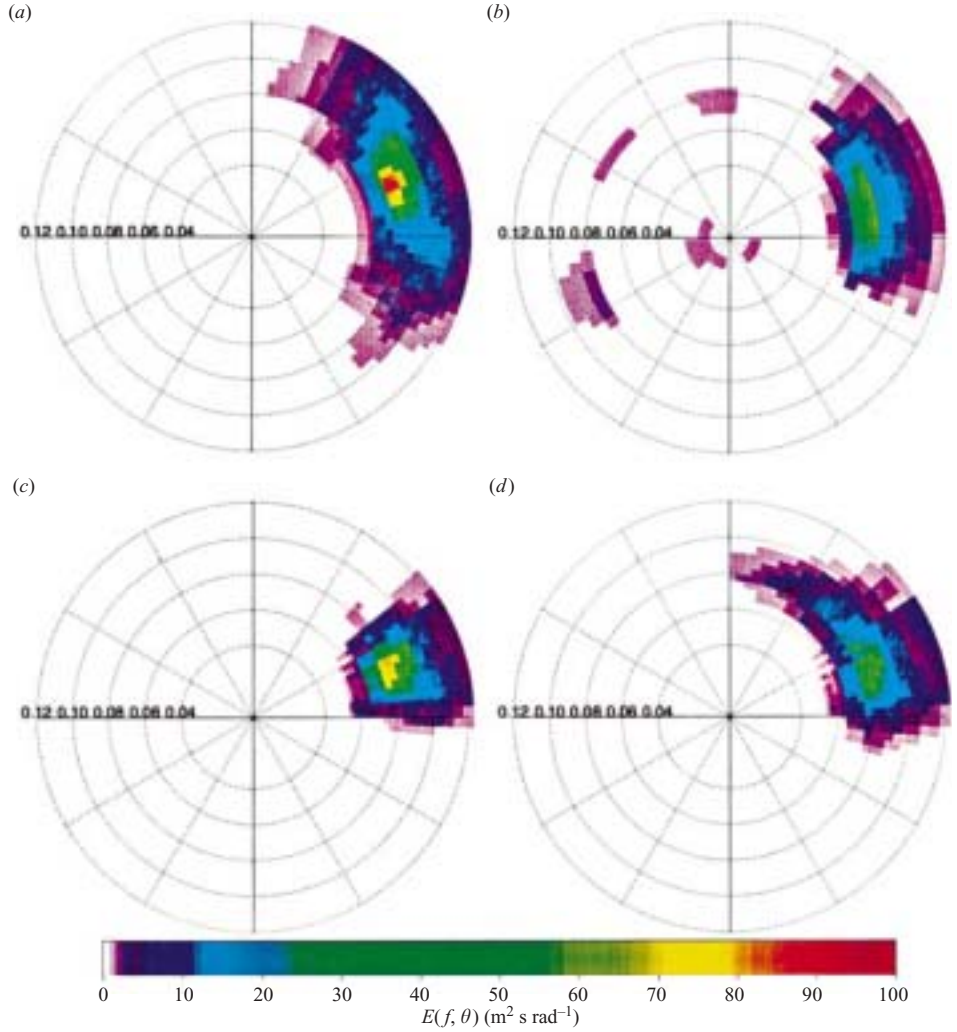

FIGURE 13. Observed wave spectra in (*a*) 49 and (*b*) 8 m depth, and predicted wave spectra in 8 m depth, (*c*) without Bragg scattering and (*d*) with Bragg scattering, based on the bottom spectrum F_1^B (figure 9*a*). Note that waves coming from the west in (*b*) are probably reflections from shore (within 1 km of the 8 m site). (*a*) $H_s = 1.50$ m; $f_p = 0.0855$ Hz; mean direction at $f_p = 72.23°$; spread at $f_p = 16.93°$. (*b*) $H_s = 1.01$ m; $f_p = 0.0805$ Hz; mean direction at $f_p = 78.73°$; spread at $f_p = 13.81°$. (*c*) $H_s = 0.93$ m; $f_p = 0.078$ Hz; mean direction at $f_p = 71.8°$; spread at $f_p = 7.49°$. (*d*) $H_s = 0.91$ m; $f_p = 0.078$ Hz; mean direction at $f_p = 66.8°$; spread at $f_p = 18.45°$.

values of l, the angular separation of the interacting wave components is small (11.5° for $k/l = 5$) and thus the energy transfers do not strongly modify a directional spectrum that is already broad. A range of interactions involving intermediate scale bottom components ($k/l = 1$ to 4) appears to dominate the scattering process (i.e. note the gradual shift of $\bar{\theta}$ and increase of σ_θ as $(k/l)_{\max}$ increases from 1 to 4 in figure 14). Predictions of σ_θ are weakly sensitive to the bathymetry smoothing scale used in ray computations, with a typical 2° difference between model runs using the original 150 m resolution grid, and the predictions presented here using a 2 km smoothed grid.

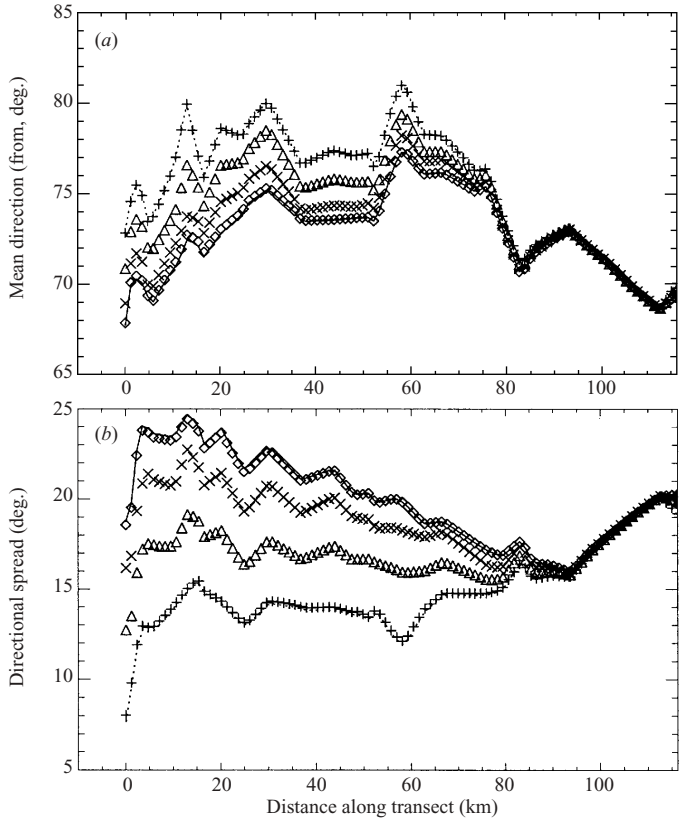

FIGURE 14. Predicted variations of (*a*) $\bar{\theta}$ and (*b*) σ_θ across the shelf for six values of the cutoff parameter $(k/l)_{\max}$: —, 5; ◇, 4; ×, 3; △, 2; +, 1; ···, 0.5 (i.e. no Bragg scattering).

5. Conclusion

The energy balance equation for random surface gravity waves, including Bragg scattering (the lowest-order resonant interactions between waves and bottom undulations), was rederived for non-stationary conditions and multiple-scale bottom topography, combining Hasselmann's (1962) perturbation expansion of the wave energy, with a ray approximation for medium variations. The bottom topography is decomposed in a large-scale topography, responsible for wave refraction and shoaling, and random undulations with smaller wavelengths (of the order of the surface wavelength), that cause Bragg scattering. The effects of the large-scale and small-scale bottom slopes, surface nonlinearity, wave non-stationarity and non-uniformity are represented by five small parameters, β, η, ε, α and γ, respectively. Using $\alpha \approx \beta \approx \gamma \approx \eta^2 \approx \varepsilon^2$, a closure of the fourth-order energy yields a spectral energy balance equation in which refraction, shoaling, and Bragg scattering processes are all of the same order ε^4.

The stochastic scattering theory was reconciled with a spectral application of deterministic theories for waves propagating over sinusoidal bars (Davies & Heathershaw 1984; Mei 1985; Dalrymple & Kirby 1986), with agreement found in the asymptotic limit of a large number of bars. These comparisons support the present derivation

of the Bragg scattering source term (2.48) which is a factor 8 and 4 smaller than expressions given by Hasselmann (1966) and Long (1973), respectively. Analysis of the detuning of wave–bottom interactions by the large–scale bottom slope β shows that the present theory is valid only for small values of $\beta/\cos^3\theta$, where θ is the wave incidence direction relative to the bedform-normal. In the present application, wave–bottom interactions corresponding to θ larger than a cutoff value $\theta_{\max}$ were neglected.

The effect of bottom scattering on swell propagation was illustrated with a hindcast for the North Carolina continental shelf using the numerical wave model CREST with high-resolution bathymetry and an efficient semi-implicit scheme to evaluate the bottom scattering source term and integrate the energy balance equation. Back-scattering of waves towards the open ocean was found to be negligible in this region. However, forward-scattering causes a diffusion of wave energy about the mean direction that results in a dramatic increase of the directional spread of the wave spectrum on the inner shelf. This weak back-scattering and strong forward-scattering is caused by the sharp roll-off of the bottom elevation spectrum at high wavenumbers. The predicted directional broadening of the swell spectrum in shallow water is qualitatively consistent with field measurements.

This research is sponsored by the Coastal Dynamics Program of the Office of Naval Research and the National Oceanographic Partnership Program (NOPP). We would like to acknowledge P. Jessen and M. Orzech (NPS) for the wave and bathymetry data analyses, the National Data Buoy Center for providing wave data for the outer shelf, and the Field Research Facility of the US Army Engineer Waterways Experiment Station's Coastal Engineering Research Center for nearshore wave and tide measurements. Permission to use these data is appreciated. Multibeam bathymetry data were acquired on board the Canadian Hydrographic vessel *Frederick G. Creed*, as part of the Bedford Institute of Oceanography contribution to SHOWEX, with the participation of F. Dobson, M. Donelan and H. Graber. T. Stanton instigated the surveys, and his involvement in, and support of the present work are greatly appreciated.

Appendix A. Derivation of $E_{2,2}(\boldsymbol{k})$

The governing equation (2.34) for $\Phi^s_{2,\boldsymbol{k}}(t)$ is an undamped forced harmonic oscillator with a resonant frequency ω given by the dispersion relation (2.28). Applying a Fourier decomposition to the right-hand side forcing terms, (2.34) can be written as a linear superposition of equations of the type

$$\frac{\mathrm{d}^2 f_1}{\mathrm{d}t^2} + \omega^2 f_1 = \mathrm{e}^{\mathrm{i}\omega' t}. \tag{A 1}$$

In order to specify a unique solution to (A 1), initial conditions must be prescribed. In the limit of large propagation distances, the initial conditions contribute a negligible bounded term to the solution. Following Hasselmann (1962), we chose $f_1(0) = 0$ and $\mathrm{d}f_1/\mathrm{d}t(0) = 0$, giving the solution

$$f_1(\omega, \omega'; t) = \frac{\mathrm{e}^{\mathrm{i}\omega' t} - \mathrm{e}^{\mathrm{i}\omega t} + \mathrm{i}(\omega - \omega')\sin(\omega t)}{\omega^2 - \omega'^2} \quad \text{for} \quad \omega'^2 \neq \omega^2, \tag{A 2}$$

$$f_1(\omega, \omega'; t) = \frac{t\mathrm{e}^{\mathrm{i}\omega' t}}{2\mathrm{i}\omega'} - \frac{\sin(\omega t)}{2\mathrm{i}\omega'\omega} \quad \text{for} \quad \omega' = \pm\omega. \tag{A 3}$$

$\Phi^s_{2,\boldsymbol{k}}(t)$ is given by

$$\Phi^s_{2,\boldsymbol{k}}(t) = \sum_{\boldsymbol{k}'} A(\boldsymbol{k},\boldsymbol{k}')B_{\boldsymbol{k}-\boldsymbol{k}'}\widehat{\Phi}^s_{1,\boldsymbol{k}'}f_1(\omega,-s\omega';t), \tag{A 4}$$

where

$$A(\boldsymbol{k},\boldsymbol{k}') = [k-\omega'^2\tanh(kH)]\frac{\boldsymbol{k}\cdot\boldsymbol{k}'}{k}. \tag{A 5}$$

The third-order energies $E_{1,2}$ and $E_{2,1}$ that result from the correlations between $\Phi^s_{1,s\boldsymbol{k}}$ and $\Phi^{-s}_{2,-s\boldsymbol{k}}$ (equation (A 4)) are found to be bounded, but the fourth-order energy $E_{2,2}$ grows with time. Substituting (A 4) in (2.16) and taking the limit (2.17) to a continuous spectrum yields the solution for $E_{2,2}(t,\boldsymbol{k})$ as defined by (2.25):

$$E_{2,2}(t,\boldsymbol{k}) = \int_0^\infty\int_0^{2\pi} A(\boldsymbol{k},\boldsymbol{k}')F^B(\boldsymbol{k}-\boldsymbol{k}')E_2(\tilde{t},\boldsymbol{k}')|f_1(\omega,-\omega';t)|^2\,\mathrm{d}k'\mathrm{d}\theta' + \ldots, \tag{A 6}$$

where $\boldsymbol{k}' = k'(\cos\theta',\sin\theta')$, and the omitted terms (...) include bounded terms forced by surface nonlinearity. Assuming that the frequency spectrum is continuous, the contribution of exact resonant interactions ($k' = k$) to (A 6) is negligible compared to contributions of near-resonant interactions ($k' \approx k$) that span a finite range of wavenumbers, and thus (A 2) can be substituted in (A 6). Changing the integration variable k' to ω', given by the dispersion relation (2.28), and removing the singularity at $\omega' = \omega$ using contour integration on the complex plane, we obtain

$$\begin{aligned} E_{2,2}(t,\boldsymbol{k}) = t\int_0^{2\pi} &\frac{4\pi\omega k^4\cos^2(\theta-\theta')}{\sinh(2kH)[2kH+\sinh(2kH)]}F^B(\boldsymbol{k}-\boldsymbol{k}')E_2(\tilde{t},\boldsymbol{k}')\,\mathrm{d}\theta' \\ &+\text{bounded terms}, \end{aligned} \tag{A 7}$$

For large t, the derivative of $E_{2,2}(t,\boldsymbol{k})$ with respect to t yields equation (2.35).

Appendix B. Derivation of $E^{\mathrm{sc}}_{3,1}(\boldsymbol{k})+E^{\mathrm{sc}}_{1,3}(\boldsymbol{k})$

The particular solution ϕ^{sc}_3 to (2.37)–(2.39) in the vicinity of $\boldsymbol{x} = \boldsymbol{0}$ can be written as

$$\phi^{\mathrm{sc}}_3(\boldsymbol{x},z,t) = \sum_{\boldsymbol{k},s}\left[\Phi^s_{3,\boldsymbol{k}}(t)\frac{\cosh(kz+kH)}{\cosh(kH)} + \Phi^{\mathrm{si},s}_{3,\boldsymbol{k}}(t)\frac{\sinh(kz+kH)}{\cosh(kH)}\right]\mathrm{e}^{\mathrm{i}\boldsymbol{k}\cdot\boldsymbol{x}}. \tag{B 1}$$

The solution for the bound component $\Phi^{\mathrm{si},s}_{3,\boldsymbol{k}}$ follows from substituting the second-order velocity potential (2.32) in the bottom boundary condition ((2.38) with term V set to zero)

$$\Phi^{\mathrm{si},s}_{3,\boldsymbol{k}}(t) = -\sum_{\boldsymbol{k}'}\frac{\boldsymbol{k}\cdot\boldsymbol{k}'}{k}B_{\boldsymbol{k}-\boldsymbol{k}'}\Phi^s_{2,\boldsymbol{k}}(t). \tag{B 2}$$

Substitution of (B 2) in the surface boundary condition ((2.39) with the right-hand side set to zero) yields the forced harmonic oscillator equation

$$\left(\frac{\mathrm{d}^2}{\mathrm{d}t^2}+\omega^2\right)\Phi^s_{3,\boldsymbol{k}} = -\sum_{\boldsymbol{k}'}\frac{\boldsymbol{k}\cdot\boldsymbol{k}'}{k}B_{\boldsymbol{k}-\boldsymbol{k}'}\left[\left(k+\tanh(kH)\frac{\mathrm{d}^2}{\mathrm{d}t^2}\right)\Phi^s_{2,\boldsymbol{k}'}(t)\right]. \tag{B 3}$$

Using (2.34) and (A 4) we have

$$\left(\frac{\mathrm{d}^2}{\mathrm{d}t^2}+\omega^2\right)\Phi^s_{3,\boldsymbol{k}} = -\sum_{\boldsymbol{k}'} A(\boldsymbol{k},\boldsymbol{k}')B_{\boldsymbol{k}-\boldsymbol{k}'}\sum_{\boldsymbol{k}''} A(\boldsymbol{k}',\boldsymbol{k}'')B_{\boldsymbol{k}'-\boldsymbol{k}''}\widehat{\Phi}^s_{1,\boldsymbol{k}''}f_1(\omega',-s\omega'';t)$$
$$-\sum_{\boldsymbol{k}'}\frac{\boldsymbol{k}\cdot\boldsymbol{k}'}{k}\tanh(kH)B_{\boldsymbol{k}-\boldsymbol{k}'}\sum_{\boldsymbol{k}''} A(\boldsymbol{k}',\boldsymbol{k}'')B_{\boldsymbol{k}'-\boldsymbol{k}''}\Phi^s_{1,\boldsymbol{k}''}(t), \qquad (B\,4)$$

where A is defined by (A 5). The only terms of (B 4) that force growing correlations with ϕ_1 are those that have a product of two factors A and equal wavenumbers $\boldsymbol{k}''=\boldsymbol{k}$, other terms force bounded correlations and can be neglected. Therefore (B 4) can be regarded as a linear combination of forced oscillator equations of the form

$$\frac{\mathrm{d}^2 f_2}{\mathrm{d}t^2}+\omega^2 f_2 = f_1(\omega',-s\omega,t). \qquad (B\,5)$$

The solution of (B 5) for $\omega'^2\neq\omega^2$ and initial conditions $f_2(0)=\mathrm{d}f_2/\mathrm{d}t(0)=0$ is

$$f_2(\omega,\omega',s;t) = -\frac{t\mathrm{e}^{\mathrm{i}s\omega t}-\sin(\omega t)/\omega}{2\mathrm{i}s\omega(\omega'^2-\omega^2)} - \frac{(\omega'+\omega)\mathrm{e}^{\mathrm{i}\omega' t}+(\omega'-\omega)\mathrm{e}^{-\mathrm{i}\omega' t}-2\omega'\mathrm{e}^{\mathrm{i}\omega t}}{2\omega'(\omega'^2-\omega^2)^2}. \qquad (B\,6)$$

Following the steps in Appendix A, we obtain

$$E^{\mathrm{sc}}_{3,1}(t,\boldsymbol{k})+E^{\mathrm{sc}}_{1,3}(t,\boldsymbol{k}) = -t\int_0^{2\pi}\frac{4\pi\omega k^4\cos^2(\theta-\theta')F^B(\boldsymbol{k}-\boldsymbol{k}')}{\sinh(2kH)[2kH+\sinh(2kH)]}E_2(\tilde{t},\boldsymbol{k})\,\mathrm{d}\theta'$$
$$+\text{bounded terms}. \qquad (B\,7)$$

Taking the derivative of (B 7) with respect to t yields equation (2.41).

Appendix C. Derivation of $E^{\mathrm{ns}}_{3,1}(\boldsymbol{k})+E^{\mathrm{ns}}_{1,3}(\boldsymbol{k})$

In the vicinity of $\boldsymbol{x}=\boldsymbol{0}$, ϕ^{ns}_3 can be written in the form

$$\phi^{\mathrm{ns}}_3 = \sum_{\boldsymbol{k},s}\frac{\cosh(kz+kH)}{\cosh(kH)}\Phi^s_{3,\boldsymbol{k}}(t)\mathrm{e}^{\mathrm{i}\boldsymbol{k}\cdot\boldsymbol{x}},$$

where $\Phi^s_{3,\boldsymbol{k}}$ satisfies

$$\left(\frac{\mathrm{d}^2}{\mathrm{d}t^2}+\omega^2\right)\Phi^s_{3,\boldsymbol{k}} = 2\mathrm{i}s\omega\frac{\partial\widehat{\Phi}^s_{1,\boldsymbol{k}}}{\partial t}\mathrm{e}^{-\mathrm{i}s\omega t}, \qquad (C\,1)$$

With the solution given by equation (A 3):

$$\Phi^s_{3,\boldsymbol{k}}(t) = -t\frac{\partial\widehat{\Phi}^s_{1,\boldsymbol{k}}}{\partial t}\mathrm{e}^{-\mathrm{i}s\omega t}. \qquad (C\,2)$$

This solution is correlated with the first-order velocity potential, giving the energy contribution at $\tilde{\boldsymbol{x}}=\boldsymbol{0}$

$$E^{\mathrm{ns}}_{3,1}(t,\boldsymbol{k})+E^{\mathrm{ns}}_{1,3}(t,\boldsymbol{k}) = -t\frac{\partial E_2(\tilde{t},\boldsymbol{k})}{\partial t}+\text{bounded term}. \qquad (C\,3)$$

Taking the derivative of (C 3) with respect to t yields (2.42).

Appendix D. Derivation of $E^{\rm he}_{3,1}(\boldsymbol{k})+E^{\rm he}_{1,3}(\boldsymbol{k})$

Terms I and II in (2.37) can be written as

$$\begin{aligned}\mathrm{I}+\mathrm{II} = \sum_{\boldsymbol{k},s} \frac{\mathrm{e}^{\mathrm{i}\boldsymbol{k}\cdot\boldsymbol{x}}}{\cosh(kH)}\{&\cosh(kz+kH)(\nabla\cdot\boldsymbol{k}_r + 2\boldsymbol{k}\cdot\nabla)\\ &+2[(z+H)\sinh(kz+kH) - H\tanh(kH)\cosh(kz+kH)]\boldsymbol{k}\cdot\nabla k_r\\ &+2[k\sinh(kz+kH) - k\tanh(kH)\cosh(kz+kH)]\boldsymbol{k}\cdot\nabla H\}\Phi^s_{1,\boldsymbol{k}}(t). \end{aligned} \tag{D 1}$$

In the vicinity of $\boldsymbol{x}=\boldsymbol{0}$, we can write the solution to (2.37) as

$$\begin{aligned}\phi^{\rm he}_3 = &\sum_{\boldsymbol{k},s} \frac{\cosh(kz+kH)}{\cosh(kH)}\left[(z+H)^2\Phi^{\mathrm{coz2},s}_{3,\boldsymbol{k}}(t) + (z+H)\Phi^{\mathrm{coz},s}_{3,\boldsymbol{k}}(t) + \Phi^s_{3,\boldsymbol{k}}(t)\right]\mathrm{e}^{\mathrm{i}\boldsymbol{k}\cdot\boldsymbol{x}}\\ &+\frac{\sinh(kz+kH)}{\cosh(kH)}\left[(z+H)\Phi^{\mathrm{siz},s}_{3,\boldsymbol{k}}(t) + \Phi^{\mathrm{si},s}_{3,\boldsymbol{k}}(t)\right]\mathrm{e}^{\mathrm{i}\boldsymbol{k}\cdot\boldsymbol{x}}, \end{aligned} \tag{D 2}$$

where

$$\begin{aligned}\Phi^{\mathrm{siz},s}_{3,\boldsymbol{k}}(t) = &\frac{-\mathrm{i}}{2k}(\Phi^s_{1,\boldsymbol{k}}(t)\nabla\cdot\boldsymbol{k}_r + 2\boldsymbol{k}\cdot\nabla\Phi^s_{1,\boldsymbol{k}}(t))\\ &+\mathrm{i}\frac{\Phi^s_{1,\boldsymbol{k}}(t)}{k}\boldsymbol{k}\cdot\left\{\left[H\tanh(k_rH) + \frac{1}{2k}\right]\nabla k_r + k\tanh(kH)\nabla H\right\}, \end{aligned} \tag{D 3}$$

$$\Phi^{\mathrm{coz2},s}_{3,\boldsymbol{k}}(t) = -\mathrm{i}\Phi^s_{1,\boldsymbol{k}}(t)\frac{\boldsymbol{k}\cdot\nabla k_r}{2k}, \tag{D 4}$$

$$\Phi^{\mathrm{coz},s}_{3,\boldsymbol{k}}(t) = -\mathrm{i}\Phi^s_{1,\boldsymbol{k}}(t)\boldsymbol{k}\cdot\nabla H, \tag{D 5}$$

and the remaining two terms follow from the bottom and surface boundary conditions. Substituting (D 2)–(D 5) in the bottom boundary condition ((2.38), with III and IV set to zero) gives

$$\Phi^{\mathrm{si},s}_{3,\boldsymbol{k}}(t) = 0. \tag{D 6}$$

Substituting (D 2)–(D 6) in the surface boundary condition ((2.39) with VI set to zero) yields a forced harmonic oscillator equation for $\Phi^s_{3,\boldsymbol{k}}(t)$:

$$\begin{aligned}&\left(\frac{\mathrm{d}^2}{\mathrm{d}t^2} + \omega^2\right)\Phi^s_{3,\boldsymbol{k}}(t) = \mathrm{i}\mathrm{e}^{-\mathrm{i}s\omega t}\left\{\left[\frac{\tanh(kH) + kH\left[1-\tanh^2(kH)\right]}{k}\right]\right.\\ &\times\left[\nabla\cdot\boldsymbol{k}_r + \boldsymbol{k}_r\cdot\nabla - 2\boldsymbol{k}\cdot\left[\left(H\tanh(kH) + \frac{1}{2k}\right)\nabla k_r + k\tanh(kH)\nabla H\right]\right]\\ &\left.+\frac{H}{k}\boldsymbol{k}\cdot\nabla k_r + \boldsymbol{k}\cdot\nabla H\right\}\widehat{\Phi}^s_{1,\boldsymbol{k}}. \end{aligned} \tag{D 7}$$

(D 7) is of the same form as (A 1) with only resonant forcing terms ($\omega' = \pm\omega$) and a solution given by (A 3). The covariance of $\Phi^{\pm}_{3,\pm\boldsymbol{k}}$ and the first-order potential, defined by (2.16), is given by

$$\begin{aligned}F^{\Phi,\mathrm{he}}_{3,1,\boldsymbol{k}} = &-t\frac{C_{\mathrm{g}}}{2k}\nabla\cdot(\boldsymbol{k}_rF^{\Phi}_{1,1,\boldsymbol{k}})\\ &+t\frac{C_{\mathrm{g}}}{k}\boldsymbol{k}\cdot\left[\left(H\tanh(kH) + \frac{1}{2k}\right)\nabla k_r + k\tanh(kH)\nabla H\right]F^{\Phi}_{1,1,\boldsymbol{k}}\\ &-\frac{t\omega}{k^2\tanh(kH)}\boldsymbol{k}\cdot(H\nabla k_r + k\nabla H)F^{\Phi}_{1,1,\boldsymbol{k}} + \text{bounded term}, \end{aligned} \tag{D 8}$$

where C_g is the group speed

$$C_g = \frac{\omega}{k_r}\left[\frac{1}{2} + \frac{k_r H}{\sinh(2k_r H)}\right], \tag{D 9}$$

and the bounded term is given by the initial conditions (the second right-hand side term in A 3). From the dispersion relation (2.28) we find

$$\nabla H = -\frac{2kH + \sinh(2kH)}{2k^2}\nabla k_r, \tag{D 10}$$

and

$$\frac{\nabla\left[C_g \tanh(k_r H)\right]}{k\tanh(kH)} = -\frac{\omega}{2k^3}\left\{3 + \frac{2kH}{\sinh(2kH)} - 2kH\tanh(kH)\right\}\nabla k_r. \tag{D 11}$$

Using (D 10), (D 11) and the definition of the Lagrangian energy spectrum $E_2(\boldsymbol{k}_r)$ (2.45), (D 8) reduces to

$$\left[E^{\mathrm{he}}_{3,1}(\boldsymbol{k}) + E^{\mathrm{he}}_{1,3}(\boldsymbol{k})\right]\Delta k_{r,x}\Delta k_{r,y} = -t\nabla\cdot(\boldsymbol{C}_g E_2(\boldsymbol{k}_r)\Delta k_{r,x}\Delta k_{r,y}) + \text{bounded terms}. \tag{D 12}$$

Writing $\boldsymbol{C}_g$ as $(C_g\cos\theta, C_g\sin\theta)$, where θ is the local ray direction, the divergence term in (D 12) can be expressed in terms of intrinsic coordinates:

$$\nabla\cdot\left[\boldsymbol{C}_g E_2(\boldsymbol{k}_r)\Delta k_{r,x}\Delta k_{r,y}\right] = \frac{\partial\left[C_g E_2(\boldsymbol{k}_r)\Delta k_{r,x}\Delta k_{r,y}\right]}{\partial r} + C_g E_2(\boldsymbol{k}_r)\Delta k_{r,x}\Delta k_{r,y}\frac{\partial\theta}{\partial n}, \tag{D 13}$$

where r and n are the local along-ray and ray-normal coordinates. Longuet-Higgins (1957, equations 6, 10 and 21) showed that (D 13) can be simplified using ray theory. Defining the small separation p of two rays that are parallel in the vicinity of $\tilde{\boldsymbol{x}} = \boldsymbol{0}$, we have

$$\frac{\partial\theta}{\partial n} = \frac{1}{p}\frac{\partial p}{\partial r} \tag{D 14}$$

and

$$\frac{\partial(pC_g\Delta k_{r,x}\Delta k_{r,y})}{\partial r} = 0. \tag{D 15}$$

Substituting (D 14) and (D 15) in (D 13), and taking the limit $|\Delta\boldsymbol{k}_r| \to 0$, we have

$$E^{\mathrm{he}}_{3,1}(\boldsymbol{k}) + E^{\mathrm{he}}_{1,3}(\boldsymbol{k}) = -tC_g\frac{\partial E_2(\boldsymbol{k}_r)}{\partial r} + \text{bounded term}. \tag{D 16}$$

Finally the derivative of (D 16) with respect to t yields (2.43).

REFERENCES

Agnon, Y. & Sheremet, A. 2000 Stochastic evolution models for nonlinear gravity waves over uneven topography. In *Advances in Coastal and Ocean Engineering*, vol. 6 (ed. P. L. F. Liu), pp. 103–131. World Scientific, Singapore.

Ardhuin, F., Herbers, T. H. C. & O'Reilly, W. C. 2001 A hybrid Eulerian–Lagrangian model for spectral wave evolution with application to bottom friction on the continental shelf. *J. Phys. Oceanogr.* **31**, 1498–1516.

Athanassoulis, G. A. & Belibassakis, K. A. 1999 A consistent coupled-mode theory for the propagation of small amplitude water waves over variable bathymetry regions. *J. Fluid Mech.* **389**, 275–301.

Belzons, M., Guazzelli, E. & Parodi, O. 1988 Gravity waves on a rough bottom: experimental evidence of one-dimensional localization. *J. Fluid Mech.* **186**, 539–558.

Belzons, M., Rey, V. & Guazzelli, E. 1991 Subharmonic Bragg resonance for surface water waves. *Europhys. Lett*. **16**, 189–194.

Benjamin, T. B., Boczar-Karakiewicz, B. & Pritchard, W. G. 1987 Reflection of water waves in a channel with corrugated bed. *J. Fluid Mech*. **185**, 249–274.

Benney, D. J. & Saffman, P. G. 1966 Nonlinear interactions of random waves in a dispersive medium. *Proc. R. Soc. Lond*. A **289**, 301–380.

Booij, N., Ris, R. C. & Holthuijsen, L. H. 1999 A third-generation wave model for coastal regions. 1. model description and validation. *J. Geophys. Res*. **104** (C4), 7649–7666.

Bretherton, F. P. & Garrett, C. J. R. 1969 Wavetrains in inhomogeneous moving media. *Proc. R. Soc. Lond*. A **302**, 529–554.

Caress, D. W. & Chayes, D. N. 1995 New software for processing sidescan data from sidescan-capable multibeam sonars. In *Proceedings of the IEEE Oceans 95 Conference*, pp. 997–1000. IEEE.

Dalrymple, R. A. & Kirby, J. T. 1986 Water waves over ripples. *J. Waterway Port Coast. Ocean Engng* **112**, 309–319.

Davies, A. G. 1979 The potential flow over ripples on the seabed. *J. Mar. Res*. **37**, 743–757.

Davies, A. G. & Heathershaw, A. D. 1984 Surface-wave propagation over sinusoidally varying topography. *J. Fluid Mech*. **144**, 419–443.

Devillard, P., Dunlop, F. & Souillard, B. 1988 Localization of gravity waves on a channel with a random bottom. *J. Fluid Mech*. **186**, 521–538.

Dulou, C., Belzons, M. & Rey, V. 2000 Laboratory study of wave bottom interaction in the bar formation on an erodible sloping bed. *J. Geophys. Res*. **105** (C8), 19 745–19 761.

Elgar, S., Herbers, T. H. C. & Guza, R. T. 1994 Reflection of ocean surface gravity waves from a natural beach. *J. Phys. Oceanogr*. **24**, 1503–1511.

Hara, T. & Mei, C. C. 1987 Bragg scattering of surface waves by periodic bars: theory and experiment. *J. Fluid Mech*. **178**, 221–241.

Hasselmann, K. 1962 On the non-linear energy transfer in a gravity wave spectrum. Part 1. General theory. *J. Fluid Mech*. **12**, 481–501.

Hasselmann, K. 1966 Feynman diagrams and interaction rules of wave–wave scattering processes. *Rev. Geophys*. **4**, 1–32.

Hasselmann, K., Barnett, T. P., Bouws, E., Carlson, H., Cartwright, D. E., Enke, K., Ewing, J. A., Gienapp, H., Hasselmann, D. E., Kruseman, P., Meerburg, A., Müller, P., Olbers, D. J., Richter, K., Sell, W. & Walden, H. 1973 Measurements of wind-wave growth and swell decay during the Joint North Sea Wave Project. *Deut. Hydrogr. Z*. **8**, 1–95, suppl. A.

Heathershaw, A. D. 1982 Seabed-wave resonance and sand bar growth. *Nature* **296**, 343–345.

Herbers, T. H. C., Elgar, S. & Guza, R. T. 1999 Directional spreading of waves in the nearshore. *J. Geophys. Res*. **104** (C4), 7683–7693.

Herterich, K. & Hasselmann, K. 1980 A similarity relation for the nonlinear energy transfer in a finite-depth gravity-wave spectrum. *J. Fluid Mech*. **97**, 215–224.

Keller, J. B. 1958 Surface waves on water of non-uniform depth. *J. Fluid Mech*. **4**, 607–614.

Kirby, J. T. 1986*a* A general wave equation for waves over rippled beds. *J. Fluid Mech*. **162**, 171–186.

Kirby, J. T. 1986*b* On the gradual reflection of weakly nonlinear Stokes waves in regions with varying topography. *J. Fluid Mech*. **162**, 187–209.

Kirby, J. T. 1988 Current effects on resonant reflection of surface water waves by sand bars. *J. Fluid Mech*. **186**, 501–520.

Kirby, J. T. 1993 A note on Bragg scattering of surface waves by sinusoidal bars. *Phys. Fluids* **5**, 380–386.

Komen, G. J., Cavaleri, L., Donelan, M., Hasselmann, K., Hasselmann, S. & Janssen, P. A. E. M. 1994 *Dynamics and Modelling of Ocean Waves*. Cambridge University Press.

Lentz, S., Guza, R. T., Elgar, S., Feddersen, F. & Herbers, T. H. C. 1999 Momentum balances on the North Carolina inner shelf. *J. Geophys. Res*. **104** (C8), 18 205–18 226.

Liu, Y. & Yue, D. K. P. 1998 On generalized Bragg scattering of surface waves by bottom ripples. *J. Fluid Mech*. **356**, 297–326.

Long, R. B. 1973 Scattering of surface waves by an irregular bottom. *J. Geophys. Res*. **78**, 7861–7870.

Longuet-Higgins, M. S. 1957 On the transformation of a continuous spectrum by refraction. *Proc. Camb. Phil. Soc*. **53** (1), 226–229.

MEI, C. C. 1985 Resonant reflection of surface water waves by periodic sandbars. *J. Fluid Mech.* **152**, 315–335.

MEI, C. C. 1989 *Applied Dynamics of Ocean Surface Waves*, 2nd edn. World Scientific.

MEI, C. C. & LIU, P. L.-F. 1993 Surface waves and coastal dynamics. *Annu. Rev. Fluid Mech.* **25**, 215–40.

MITRA, A. & GREENBERG, M. D. 1984 Slow interaction of gravity waves and a corrugated sea bed. *J. Appl. Mech.* **51**, 251–255.

MUNK, W. H. & TRAYLOR, M. A. 1947 Refraction of ocean waves: a process linking underwater topography to beach erosion. *J. Geol.* **55**, 1–26.

NEWELL, A. C. & AUCOIN, P. J. 1971 Semidispersive wave systems. *J. Fluid Mech.* **49**, 593–609.

O'REILLY, W. C. & GUZA, R. T. 1993 A comparison of two spectral wave models in the Southern California Bight. *Coastal Engng* **19**, 263–282.

PIERSON, JR, W. J. & MOSKOWITZ, L. 1964 A proposed spectral form for fully developed wind seas based on the similarity theory of S. A. Kitaigorodskii. *J. Geophys. Res.* **69**, 5181–5190.

PRESS, W. H., TEUKOLSKY, S. A., VETTERLING, W. T. & FLANNERY, B. P. 1992 *Numerical Recipes*, 2nd edn. Cambridge University Press.

PRIESTLEY, M. B. 1965 Evolutionary and non-stationary processes. *J. R. Statist. Soc.* B **27**, 204–237.

PRIESTLEY, M. B. 1981 *Spectral Analysis and Time Series.* Academic Press.

RICHTER, K., SCHMALFELDT, B. & SIEBERT, J. 1976 Bottom irregularities in the North Sea. *Deut. Hydrogr. Z.* **29**, 1–10.

WAMDI GROUP 1988 The WAM model – a third generation ocean wave prediction model. *J. Phys. Oceanogr.* **18**, 1775–1810.

WILLEBRAND, J. 1975 Energy transport in a nonlinear and inhomogeneous random gravity wave field. *J. Fluid Mech.* **70**, 113–126.